Final Report
RF Project 2033

BOUNDARY LAYER STUDIES IN AN ARC-HEATED WIND TUNNEL

Stuart L. Petrie

Department of Aeronautical &
Astronautical Engineering

National Aeronautics & Space Administration
Washington D.C. 20546

Grant No. NGR 36-008-032

RF Project 2033

Report No. 5

FINAL

REPORT

By

THE OHIO STATE UNIVERSITY
RESEARCH FOUNDATION

1314 KINNEAR RD.
COLUMBUS, OHIO 43212

To NATIONAL AERONAUTICS AND SPACE ADMINISTRATION
Washington D. C. 20546
Grant No. NGR 36-008-032

On BOUNDARY LAYER STUDIES IN AN ARC-HEATED TUNNEL

For the period May 1, 1965 - October 31, 1967

Submitted by Stuart L. Petrie
The Aeronautical and Astronautical Research Laboratory
Department of Aeronautical and Astronautical Engineering

Date April 29, 1968

FOREWORD

These studies were conducted at The Aeronautical and Astronautical Research Laboratory of The Ohio State University. The research was supported by The National Aeronautics and Space Administration under NASA Grant NGR-36-008-032. Dr. Robert Graham, of the Lewis Research Center, Cleveland, Ohio, served as the technical monitor.

ABSTRACT

Experimental and theoretical studies of the laminar boundary layer in the nozzle of an arc-heated wind tunnel are reported. Measurements were conducted with air as the effluent, with stagnation enthalpies from 2000 to 6000 Btu/lb at stagnation pressures near 1 atm. The data were obtained under conditions such that the boundary layer composed a major portion of the flow field. Boundary layer thicknesses and detailed velocity and temperature profiles were obtained with an electron beam and various probes. Theoretical analyses for predicting thickness distributions and boundary layer profiles were examined for applicability in high-enthalpy nozzle flows. The method of Cohen and Reshotko was found to yield displacement thicknesses within 4% of the measured values when the effects of displacement interaction were included. The technique of Beckwith and Cohen and Pohlhausen energy and momentum integral methods were found to be unsatisfactory for estimating the thickness distributions. Inclusion of transverse curvature in the analyses demonstrated that superior thickness results are obtained with a consistent treatment of the curvature effects.

Comparison of the theoretical and experimental boundary layer profiles show that the temperature profiles are very sensitive to the technique of computation. Flat plate theories were found to greatly over-estimate the peak temperature in the boundary layer. Transverse curvature effects were found to have a minor influence on the profiles. Good agreement of the experimental profiles with those computed with the locally similar form of the boundary layer equations was obtained when the proper value for the pressure gradient parameter (β) was employed.

Measurement of the temperature and density profiles with several techniques and the molecular nitrogen vibrational temperature profiles obtained with the electron beam indicated that there was little chemical activity within the boundary layer. However, an anomolous distribution of vibrational temperature was obtained suggesting the existence of a wall effect on the vibrational relaxation process.

TABLE OF CONTENTS

LIST OF FIGURES

LIST OF SYMBOLS

a	speed of sound
a_i	coefficient of $(\eta)^i$ in Pohlhausen velocity polynomial
$A(\xi)$	transformation function defined by Eq. (17)
A	constant defined by Eq. (70)
b_i	coefficient of $(\eta)^i$ in Pohlhausen enthalphy polynomial
B	constant defined by Eq. (70)
$c(x)$	transformation function defined by Eq. (60)
C	density-viscosity ratio,
D	nozzle diameter
E	function defined by Eq. (87)
f	transformed steam function, $f' = u/u_1$
g	enthalpy ratio, $g = S/S_W + 1$
h	static enthalpy
H	stagnation enthalpy, $H = h + \frac{1}{2} u^2$
H	form factor, $H_{tr} = \delta^*_{tr}/\theta_{tr}$
K	$(3\gamma-1)/2(\gamma-1)$
ℓ	shear parameter, $\ell = \frac{\theta_{tr}}{U_1}(U_y)_W$
M	Mach number
n	correlation number, $n = -\frac{U_{1x}}{\nu_o}\theta^2_{tr}$
N	momentum parameter, $N = 2[n(H_{tr}+2) + \ell]$
p	static pressure
p_{T_2}	pitot pressure
P_R	Prandtl number

q	heat transfer rate, $q = k_W(\partial T/\partial y)_W$
r	distance normal to axis of symmetry
R	$(r/r_W)^2$
S	enthalpy function, $S = \frac{h_W}{H_1} - 1$
T	static temperature
u	velocity in x-direction
U	transformed velocity in X-direction
v	velocity in y-direction
V	transformed velocity in Y-direction
x	coordinate along nozzle wall
X	transformed x-coordinate, $X = \int_0^x \lambda \frac{a_1}{a_0} \frac{p_1}{p_0} r_W^2 \, dx$
y	coordinate normal to nozzle wall
Y	transformed y-coordinate, $Y = \frac{a_1}{a_0} \int_0^y \frac{\rho}{\rho_0} r \, dy$
Z	compressibility factor
α	nozzle half angle
β	pressure gradient parameter
γ	ratio of specific heats
Γ	function defined by Eq. (81)
ξ	transformed X-coordinate, $\xi = X$
$\overline{\xi}$	function defined by Eq. (25)
η	transformed Y-coordinate, $\eta = Y/\sqrt{\nu_0 A(\zeta)}$
θ	momentum thickness
μ	viscosity
ν	dynamic viscosity, $\nu = \mu/\rho$
δ	velocity thickness
δ^*	displacement thickness

δ_H	enthalpy thickness
ϕ	enthalpy function $\phi = 1 - S/S_W$
ρ	mass density

Subscripts

o	stagnation conditions
1	denotes conditions at outer edge of boundary layer
2	denotes quantities for thin boundary layers
w	wall conditions
tr	denotes quantities in (X,Y) coordinate system

A coordinate variable which appears as a subscript denotes partial differentation with respect to the variable.

Superscripts

*	conditions at a sonic throat

LAMINAR BOUNDARY LAYERS IN HIGH ENTHALPY FLOWS

I. INTRODUCTION

There is considerable interest in the properties of laminar boundary layers in high-enthalpy flows. Successful nozzle design for high-enthalpy test facilities necessitates accurate techniques for the prediction of boundary layer growth rates and wall heat transfer rates. Further, the aerodynamic characteristics of flight vehicles at high altitudes are controlled by boundary layer phenomena.

Various approximate methods have been proposed for analysis of these high-enthalpy laminar boundary layers. However, the analyses are complicated by the possible existance of thermochemical nonequilibrium in the effluent and by the possible influences of transverse curvature effects.

The purpose of this paper is to present the results of experimental and theoretical analyses of the high-speed laminar boundary layer in the nozzle of an arc-heated wind tunnel. Boundary layer growth rates and profiles of velocity, density, molecular concentration, static temperature, and vibrational temperature were measured at various axial locations in the supersonic portion of the nozzle flow field. The measurements were obtained in expanded arc-heated air flows under conditions such that the boundary layer comprised a major portion of the flow field. In addition, the stagnation enthalpy of the flow was sufficiently high to cause almost complete dissociation of molecular oxygen at an equilibrium stagnation point and significant nonequilibrium in the vibrational energy mode of molecular nitrogen.

The experimental results are compared with those from various theoretical methods. While the empirical formulas of Burke and Bird[1] and Edenfield and Boudreau[2] give reasonable estimates of boundary layer thicknesses, other techniques of analysis must be employed to obtain more detailed information. The theoretical methods include application of Pohlhausen techniques,[3] methods utilizing the concept of local similarity,[4,5] and finite difference integration of the boundary layer equations.[6,7,8]

High enthalpy nozzle flows provide extreme ranges of conditions for development of the boundary layer. In the subsonic region of the flow, there are large changes in static temperature through the layer so that changes in fluid properties (i.e., viscosity-density product) must be considered. In the region near the nozzle throat there are extremely large axial gradients in the inviscid flow properties. These large gradients invalidate the assumption of local similarity and may influence the boundary layer at large distances downstream of the throat. In the supersonic flow, the boundary layer thickness frequently becomes so large that displacement interaction and transverse curvature effects become significant.

Numerical schemes for solving the boundary layer equations retaining the nonsimilar and curvature terms have been developed. However, when displacement interaction must be considered, a time-consuming iterative technique of solution must be employed. Hence, a rapid and accurate method of predicting boundary layer growth rates and detailed profile parameters would be extremely desirable.

A computation scheme employing the separability of curvature and displacement interaction effects is developed here. The results from this theoretical method and from those commonly employed for laminar boundary layer analysis are compared with the experimental results. These comparisons demonstrate the relative applicability of the theoretical methods and indicate the importance of the influences of prior history, curvature, and displacement interaction in the development of the boundary layer. While the main emphasis here is on nozzle boundary layers, the results are applicable to any axisymmetric geometry.

For the range of wind tunnel stagnation conditions investigated, the studies previously reported[9,10] show that the gas expands in the inviscid flow with a frozen chemical composition. The results discussed here also indicate that there is little chemical activity within the boundary layer. Hence, the influences of chemical reactions and species diffusion are not considered in formulation of the theoretical methods of boundary layer analysis.

Results obtained in the free jet a small distance downstream of the nozzle exit were reported previously.[11] These studies have been extended to include the boundary layer inside the nozzle at various axial stations and the results are reported here. Data from Reference 11 are included for purposes of discussion and completeness.

II. THEORETICAL ANALYSIS

A. BOUNDARY LAYER EQUATIONS

The theoretical methods of predicting boundary layer characteristics in axisymmetric nozzles are described in this section. The basic equations for thick laminar layers, including the effects of transverse curvature, have been discussed by Probstein and Elliott.[14] Referring to Fig. 1, these equations are:

$$(\rho u r)_x + (\rho v r)_y = 0 \quad , \tag{1}$$

$$\rho(u u_x + v u_y) = \rho_1 u_1 u_{1x} + \frac{1}{r}(\mu r u_y)_y \quad , \quad \text{and} \tag{2}$$

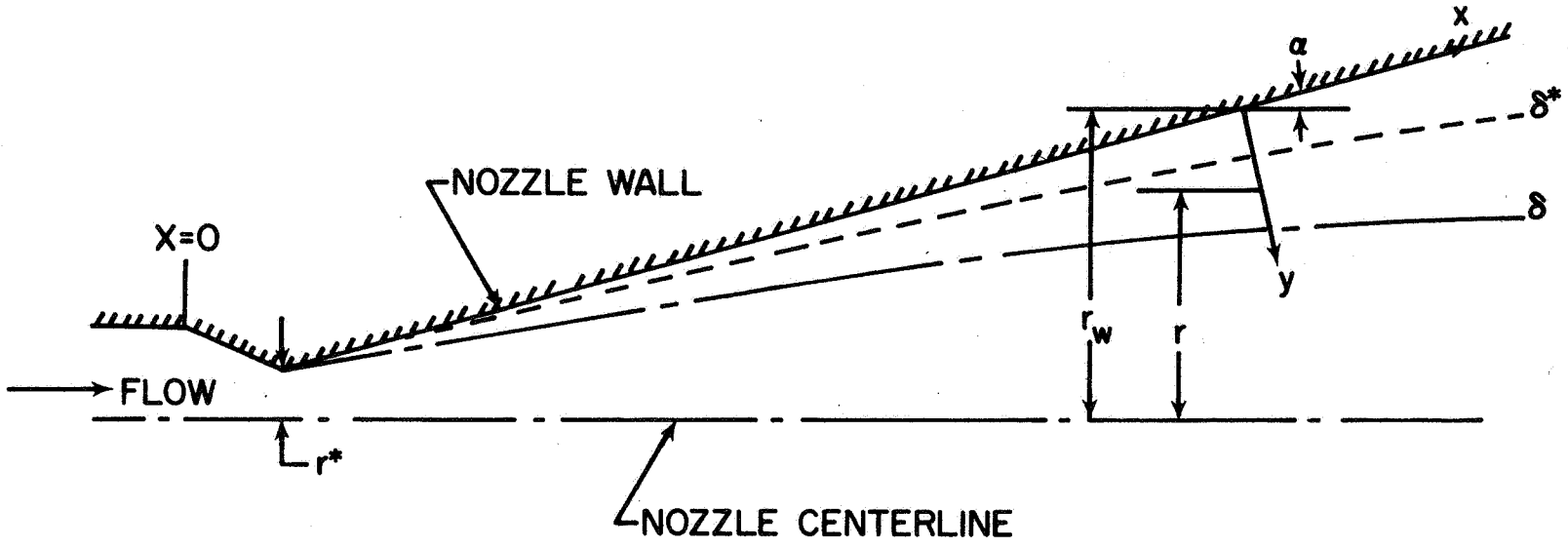

Fig. 1 - Coordinate System

$$\rho(uH_x+vH_y) = \frac{1}{r}\left[\left(\frac{\mu r}{P_R} H_y\right)_y + \left\{ \mu \left(1 - \frac{1}{P_R}\right) ruu_y \right\}_y\right] \quad , \qquad (3)$$

where

$$H = h + \tfrac{1}{2}u^2 \quad . \qquad (4)$$

Various techniques for solution of the boundary layer equations have been discussed in the literature. These techniques may be grouped into three general catagories: (1) numerical integration, (2) integral methods, and (3) similarity analysis. However, in most analyses the second-order transverse curvature (TVC) effect is neglected and no attempt is made to include the interaction of the boundary layer with the external inviscid flow. In this discussion, the transverse curvature terms will be retained in the boundary layer equations and techniques for including displacement interaction will be examined.

The boundary layer equations can be rewritten by introducing a modified form of Stewartson's[12] transformation defined by

$$X = \int_0^x \lambda \frac{a_1}{a_o} \frac{p_1}{p_o} r_w^2 \, dx \qquad (5)$$

and

$$Y = \frac{a_1}{a_o} \int_0^y \frac{\rho}{\rho_o} r \, dy \quad , \qquad (6)$$

where λ is defined by the viscosity law[4]

$$\frac{\mu}{\mu_o} = \lambda \frac{T}{T_o} \quad . \qquad (7)$$

A stream function is defined such that

$$\psi_x = - \frac{\rho}{\rho_o} vr \qquad (8)$$

and

$$\psi_y = \frac{\rho}{\rho_o} ur \quad . \qquad (9)$$

Applying Eqs. (5)-(9) to the boundary layer Eqs. (1-3) results in

$$U_x + V_y = 0 \quad , \qquad (10)$$

$$UU_x + VU_y = (1+S)U_1U_{1x} + \nu_o(RU_y)_y \quad , \quad \text{and} \tag{11}$$

$$UH_x + VH_y = \frac{\nu_o}{P_R}\left[(RH_y)_y + (P_R-1)\frac{T_1}{T_o}(RUU_y)_y\right], \tag{12}$$

where

$$S = \frac{H}{H_1} - 1 \quad , \tag{13}$$

$$U = \psi_y = \frac{a_o}{a_1}u \quad , \tag{14}$$

$$V = -\psi_x \quad , \quad \text{and} \tag{15}$$

$$R = (r/r_w)^2 = (1-y\cos\alpha/r_w)^2 \tag{16}$$

Equations (5)-(15) are the same as those of Cohen and Reshotko[4] except for the inclusion of the TVC term, R. These equations can be written in a form suitable for similarity analysis by introducing the transformation.

$$\psi = \sqrt{\nu_o}A(\xi)U_1 f(\xi,\eta) \quad , \tag{17}$$

$$\xi = X \quad , \tag{18}$$

$$\eta = Y/\sqrt{\nu_o}A(\xi) \quad , \tag{19}$$

where $A(\xi)$ is an arbitrary scaling factor. Applying Eqs. (17)-(19) to the incompressible form of the boundary layer Eqs. (10-12) results in

$$(Rf_{\eta\eta})_\eta + A(U_1A)_\xi f f_{\eta\eta} + A^2U_{1\xi}(1+S-f_\eta^2) = A^2U_1(f_\eta f_{\eta\xi} - f_{\eta\eta}f_\xi) \tag{20}$$

and

$$(RS_\eta/P_R)_\eta + A(U_1A)_\xi f S_\eta + \frac{u_1^2}{H_1}\left[R\left(1-\frac{1}{P_R}\right)f_\eta f_{\eta\eta}\right]_\eta = A^2U_1(f_\eta S_\xi - f_\xi S_\eta) \tag{21}$$

with boundary conditions

$$\begin{aligned} &\eta = 0,\ f = f_\eta = 0 \quad ; \quad S = S_w = T_W/T_o - 1 \\ &\eta = \infty,\ f_\eta = 1 \quad ; \quad S = 0 \quad . \end{aligned} \tag{22}$$

An alternate form of the boundary layer equations can be obtained with a modification of the Levy-Lees transformation suggested by the work of Beckwith and Cohen.[5] Let

$$\xi = \int_0^x \rho_w \mu_w u_1 r_w^2 dx \tag{23}$$

and

$$\eta = \frac{u_1}{\sqrt{2(\xi-\bar{\xi})}} \int_0^y \rho \, r dy \quad . \tag{24}$$

With a transformed steam function defined as

$$f(\xi,\eta) = \psi/\sqrt{2(\xi-\bar{\xi})} \tag{25}$$

$$\rho \, ur = \psi_y \tag{26}$$

$$\rho \, vr = - \psi_x \tag{27}$$

the boundary layer equations become

$$(CRf_{\eta\eta})_\eta + (1-d\bar{\xi}/d\xi)ff_{\eta\eta} + \beta(1+S-f_\eta^2) = 2(\xi-\bar{\xi})(f_\eta f_{\eta\xi} - f_\xi f_{\eta\eta}) \tag{28}$$

and

$$(CRS_\eta/P_R)_\eta + (1-d\bar{\xi}/d\xi)fS_\eta + \frac{u_1^2}{H_1}\left[CR\left(1-\frac{1}{P_R}\right)f_\eta f_{\eta\eta}\right]_\eta = 2(\xi-\bar{\xi})(f_\eta S_\xi - f_\xi S_\eta) \quad , \tag{29}$$

where $\bar{\xi}$ is an arbitrary scaling factor and

$$\beta = \frac{2(\xi-\bar{\xi})}{u_1}\frac{H_1}{h_1}\frac{du_1}{dx} \quad , \tag{30}$$

$$C = \rho\mu/\rho_w\mu_w \quad , \tag{31}$$

$$R = 1 - A_2 \int_0^\eta \frac{T}{T_1} d\eta \quad , \quad \text{and} \tag{32}$$

$$A_2 = \frac{2 \cos \alpha \sqrt{2(\xi-\bar{\xi})}}{\rho_1 u_1 r_w^2} \quad . \tag{33}$$

Equations (28) and (29) and the transformation defined by Eq. (23) and (24) differ from those of Beckwith and Cohen since transverse curvature effects are included through the appearance of R.

Both sets of transformed equations given above are exact within the framework of boundary layer theory. The "nonsimilar" terms have been retained, transverse curvature effects have not been neglected, and the Prandtl number has not been assumed constant. However, the chemical composition of the flow within the boundary layer has been assumed constant.

B. GENERAL METHOD OF SOLUTION

The boundary layer displacement thickness, skin friction, and heat transfer rate are obtained by solving either Eq. (20)-(21) or (28)-(33) for the boundary layer profiles. A general solution of these equations necessitates numerical integration of their finite-difference equivalents. In addition, provisions must be made to account for the interaction of the boundary layer with the inviscid flow.

To account for this displacement interaction, the boundary layer displacement thickness must be computed and revised inviscid flow properties must be obtained. The revised properties are determined by decreasing the effective nozzle radius by an amount equal to the boundary layer displacement thickness. The revision of the inviscid flow properties requires recomputation of the boundary layer displacement thickness and an iterative scheme of solution is required. For the range of stagnation conditions considered here, five iterations are necessary before four-place accuracy in displacement thickness is obtained.

The numerical techniques of Smith and Clutter[7] appear well-suited for numerical computation of nozzle boundary layer properties including TVC effects. The stream-wise derivatives in the transformed boundary layer equations are replaced by their finite difference equivalents and boundary layer profiles are obtained at various x-locations. Since the transformation is applied mainly for numerical convenience, its detailed form is not important. However, in high-gradient regions of the flow, the step-size in the direction of flow must be reduced to maintain accuracy. This small step-size coupled with the need for iteration to properly account for displacement interaction can lead to prohibitively long computing times.

To circumvent the long computing time required for "exact" numerical solution of the boundary layer equations with displacement interaction, an approximate method based on the separability of interaction and curvature effects has been developed. In this method, the concept of local similarity in the boundary layer is employed.

The conditions under which similar solutions of the boundary layer equations can be found are determined by requiring that f be a function only of η. Substitution of this condition in Eqs. (20) and (21) gives

$$(Rf'')' + A(U_1A)_\xi ff'' + A^2U_{1_\xi}(1+S-f'^2) = 0 \qquad (34)$$

and

$$\left(\frac{R}{P_R}S'\right)' + A(U_1A)_\xi fS' + \frac{u_1^2}{H_1}\left[R\left(1-\frac{1}{P_R}\right)ff''\right]' = 0 \quad . \qquad (35)$$

With constant Prandtl number, similarity exists only under the following conditions:

(a) $A(U_1A)_\xi$ = constant ,

(b) $\beta = A^2U_{1_\xi}$ = constant ,

(c) $R = 1 - \dfrac{2\sqrt{\nu_o}A\cos\alpha}{r_w^3}\dfrac{a_o}{a_1}\dfrac{\rho_o}{\rho_1}\displaystyle\int_0^\eta \frac{T}{T_1}d\eta$ = function of η alone ,

(d) $P_R = 1$ or u_1^2/H_1 = constant, and

(e) S_W = constant .

The constants in either (a) or (b) can be assigned an arbitrary value with no loss of generality.

Accordingly, let

$$A(U_1A)_\xi = 1 \quad . \qquad (36)$$

Solution of Eq. (36) yields

$$\beta = -\frac{2(T_o/T_1)(p_e/p_1)}{\rho_1 u_1^3 r_w^2}\left[\int_0^x \frac{p_1}{p_o}u_1 r_w^2\,dx\right]\frac{dp}{dx} \quad . \qquad (37)$$

The similarity conditions then become:

$$\beta = A^2dU_1/dx = \text{constant} \quad , \qquad (38)$$

$$A_1 = \frac{2\sqrt{\nu_o}\cos\alpha}{r_w^3}\frac{a_o}{a_1}\frac{\rho_o}{\rho_1}A = \text{constant} \quad , \qquad (39)$$

$$A_3 = \frac{H_1}{h_1}A_1 = \text{constant} \quad , \qquad (40)$$

$$P_R = 1 \text{ or } u_1^2/H_1 = \text{constant} \quad , \quad \text{and} \tag{41}$$

$$S_w = \text{constant} \quad . \tag{42}$$

With β given by Eq. (37), A, A_1, and A_3 can be given in terms of integrals over the external flow parameters. The similarity equations reduce to

$$(Rf'')' + ff'' + \beta(1+S-f'^2) = 0 \tag{43}$$

and

$$(RS')' + P_R fS' + \frac{u_1^2}{H_1}(P_R-1)(Rf'f'')' = 0 \tag{44}$$

where

$$R = 1 - A_1 \int_0^\eta \frac{T}{T_1}\, d\eta \tag{45}$$

and

$$\frac{T}{T_1} = f'^2 + \frac{A_3}{A_1}(1+S-f'^2) \quad . \tag{46}$$

When the boundary layer thickness, δ, is such that transverse curvature effects are negligible and $R = 1$, Eq. (43)-(46) reduce to

$$f''' + ff'' + \beta(1+S-f'^2) = 0 \tag{47}$$

and

$$S'' + P_R fS' + \frac{u_1^2}{H_1}(P_R-1)(f'f'')' = 0 \tag{48}$$

and the conditions for similarity become

$$\beta = A^2 dU_1/dx = \text{constant} \quad , \tag{49}$$

$$P_R = 1 \text{ or } u_1^2/H_1 = \text{constant} \quad , \quad \text{and} \tag{50}$$

$$S_w = \text{constant} \quad . \tag{51}$$

The types of flow for which similar solutions of Eq. (43)-(46) exist have been examined by Yasuhara.[13] The existance of similar solutions for Eq. (47)-(48) has been discussed by Cohen and Reshotko.[4] In a general flow field, these similarity conditions cannot be satisfied. However, solutions can be obtained with the assumption of local similarity.

When the assumption of local similarity is made, the flow properties are assumed to vary slowly in the stream-wise (ξ) direction. The nonsimilar terms on the right-hand sides of the momentum equation (20) and energy equation (21) are dropped. The ξ-dependent terms on the left-hand sides of the equations are assumed to take local values and the boundary layer equations are considered as ordinary differential equations in η with ξ as a parameter. Thus, the history of the boundary layer is ignored except for its influence in the calculation of ξ.

With the assumption of local similarity and retaining the TVC terms, the boundary layer equations reduce to Eq. (43) and (44). The quantities β, A_1, A_2, and u_1^2/H_1 are considered as parameters in the solution. With the neglect of TVC effects, Eq. (47) and (48) result. Profile solutions are obtained from these equations at various locations in the flow field and the solutions are patched together to give the variation of displacement thickness, surface skin friction, etc.

It is clear from Eq. (47)-(51) that when transverse curvature effects are neglected and P_R is set equal to unity, universal solutions for the boundary layer profiles can be obtained in terms of the parameters β and S_w. Hence, profile solutions can be tabulated in terms of these two parameters independent of the detailed free-stream properties. Once the value of β is determined, these profile tabulations can be consulted to obtain the complete solution. However, when the transverse curvature terms are retained in the boundary layer equations, no universal solutions exist. The profiles depend explicitly on the external flow properties through the parameters A_1 and A_3. Hence detailed profiles must be computed at each stream-wise location.

When significant displacement interaction effects must be considered, the application of local similarity with transverse curvature appears to provide no particular advantage over straightforward numerical solution of the boundary layer equations. With each correction to the inviscid flow introduced to account for displacement interaction, new profile solutions must be obtained and these must be patched together to give the revised displacement thickness distribution.

The numerical integration of the boundary layer equations can be simplified considerably by employing the separability of curvature and displacement interaction effects. Probstein and Elliott[14] and Hayes and Probstein[15] have shown that in certain simplified cases transverse curvature does not alter the displacement thickness to first-order. This is exemplified by the calculations for external boundary layers by Jaffe, Lind, and Smith,[18] where transverse curvature effects were found to markedly alter the profiles and surface skin friction distribution while causing only a minor change in the displacement thickness from that calculated neglecting transverse curvature. Thus, the boundary layer displacement thickness and the displacement interaction effects can be computed neglecting the curvature terms. With the major effects of interaction thus accounted for, the boundary layer equations including

curvature and the "nonsimilar" terms may be integrated numerically to obtain skin friction, heat transfer rate, detailed boundary layer profiles, and the revised displacement thickness. Since curvature does not alter the displacement thickness to first-order, the revised thickness differs little from that computed without curvature and there is no need to alter the free-stream flow and repeat the solution.

Numerical integration of the boundary layer equations for high-enthalpy nozzle flows presents extreme numerical difficulties. The set of equations constitutes a boundary value problem with boundary conditions specified at the wall and at the outer edge of the layer. The integration usually is accomplished by assuming values for the unknown derivatives at the wall, $f''(0)$ and $S'(0)$. The resulting solution at the outer edge is examined and the assumed values of the wall derivatives are readjusted until the outer boundary conditions are satisfied. In the region of the nozzle throat, pressure gradient parameters (β) in excess of 10 can result. For these high values of β the solution of the transformed momentum equation is extremely sensitive to the assumed value for $f''(0)$. A limited number of solutions of the set of nonsimilar equations have been obtained in the course of these studies and it has been found that divergent solutions for f' oscillating between $\pm\infty$ result from as little as a $10^{-5}\%$ change in $f''(0)$. However, because of the nature of the nozzle flow, adequate boundary layer thicknesses can be obtained without detailed numerical integration of the nonsimilar boundary layer equations.

The nonsimilar nature of the flow field is expected to be most important in the region of the nozzle throat where the flow properties vary rapidly with distance along the nozzle centerline. However, in the throat region the boundary layer thicknesses are extremely small because of the relatively high Reynolds number and large amounts of wall cooling. Hence, the errors in the boundary layer thickness caused by neglect of the nonsimilar terms are expected to be a negligible fraction of the nozzle radius. In the supersonic and hypersonic flow regions where the boundary layer thicknesses are large, the changes in the pressure gradient parameter in the flow direction are small so that a theory employing local similarity is expected to be valid. Thus, the need for a detailed numerical integration of the boundary layer equations can be avoided by the application of local similarity.

Boundary layer thicknesses obtained from a technique employing the assumption of local similarity and properly corrected for transverse curvature and displacement interation effects are expected to be sufficiently accurate. However, the technique may not give adequate boundary layer profiles. The nonsimilar nature of the flow near the throat will influence the boundary layer in the downstream regions and may alter the shape of the profiles. The comparisons of the experimental and theoretical profiles presented in later sections allow some conclusions regarding the influence of this prior history on the profiles.

C. BOUNDARY LAYER THICKNESS DETERMINATION

The boundary layer thicknesses are determined with a modification of the method due to Cohen and Reshotko.[4] In this technique, the pressure gradient parameter is obtained from a correlation employing the "incompressible" momentum integral equation. This equation is obtained by integrating Eq. (11) from Y = 0 to Y = ∞ with the result

$$\frac{d\theta_{tr}}{dx} + \frac{U_{1x}}{U_1}\left(2\theta_{tr} + \delta^*_{tr}\right) = \frac{\nu_o}{U_1^2}\left(U_y\right)_w \quad , \tag{52}$$

where the transformed momentum thickness, θ_{tr}, and transformed displacement thickness, δ^*_{tr}, are defined as

$$\theta_{tr} = \int_0^\infty \frac{U}{U_1}\left(1 - \frac{U}{U_1}\right) dY \tag{53}$$

and

$$\delta^*_{tr} = \int_0^\infty \left(1 + S - \frac{U}{U_1}\right) dY \quad . \tag{54}$$

It is particularly noteworthy that Eq. (52)-(54) are exactly the same as those developed by Cohen and Reshotko without consideration of transverse curvature effects.

Equation (52) is rewritten in terms of dimensionless wall shear and transformed velocity parameters defined as:

Shear Parameter,

$$\ell = \frac{\theta_{tr}}{U_1}\left(U_y\right)_w \quad ; \tag{55}$$

Correlation number,

$$n = -\frac{U_{1x}}{\nu_o}\theta_{tr}^2 \quad . \tag{56}$$

With these parameters, Eq. (52) can be written as

$$-U_1 \frac{d}{dx}\left(\frac{n}{U_{1x}}\right) = 2\left[n(H_{tr}+2) + \ell\right], \tag{57}$$

where $H_{tr} = \delta^*_{tr}/\theta_{tr}$ is the form factor for incompressible flow.

The actual displacement and momentum thicknesses are defined in terms of mass and momentum defects within the boundary layer.

The mass defect is written as

$$\int_0^{\delta^*} 2\pi r\rho_1 u_1 dy = \int_0^{\infty} 2\pi r(\rho_1 u_1 - \rho u) dy \quad ,$$

from which δ^* is obtained as

$$\delta^* - \frac{\delta^{*2} \cos \alpha}{2r_w} = \int_0^{\infty} \frac{r}{r_w} \left(1 - \frac{\rho u}{\rho_1 u_1}\right) dy \quad . \tag{58}$$

Transforming the integral from y to η with Eq. (6) and (19) and solving for δ^* gives

$$\delta^* = \frac{r_w}{\cos \alpha} \left[1 - \left(1 - \frac{2 \cos \alpha}{r_w} \delta_2^*\right)^{\frac{1}{2}}\right] \quad , \tag{59}$$

where

$$\delta_2^* = C(x) \int_0^{\infty} \left(\frac{\rho_1}{\rho} - \frac{u}{u_1}\right) d\eta$$

and (60)

$$C(x) = \left[\sqrt{\nu_o} A(x)/r_w\right] \frac{a_o}{a_1} \frac{\rho_o}{\rho_1} \quad .$$

In a similar fashion, the momentum defect in the boundary layer is written as

$$\int_0^{\theta} 2\pi r\rho_1 u_1^2 dy = \int_0^{\infty} 2\pi r\rho(u_1 u - u^2) dy \quad . \tag{61}$$

Solution of Eq. (61) gives the momentum thickness as

$$\theta = \frac{r_w}{\cos \alpha} \left[1 - \left(1 - \frac{2 \cos \alpha}{r_w} \theta_2\right)^{\frac{1}{2}}\right] \quad , \tag{62}$$

where

$$\theta_2 = C(x) \int_0^{\infty} \frac{u}{u_1} \left(1 - \frac{u}{u_1}\right) d\eta \quad . \tag{63}$$

The quantities δ_2^* and θ_2 are the thicknesses for thin axisymmetric boundary layers and are calculated by the method of Cohen and Reshotko. In this technique, it is assumed that Eq. (47) and (48) with the Prandtl number set equal to unity adequately describe the boundary layer. Thus, the profile parameters are obtained from the following equations:

$$f''' + ff'' + \beta(1+S-f'^2) = 0 \tag{64}$$

and

$$S'' + fS' = 0 \tag{65}$$

For given values of β and S_w, Eq. (64) and (65) can be solved and the profile parameters n, ℓ, and H_{tr} can be determined from the relationships

$$\ell = f''(0)\int_0^\infty f'(1-f')d\eta \tag{66}$$

$$n = -\left[\frac{\ell}{f''(0)}\right]\beta \quad , \quad \text{and} \tag{67}$$

$$H_{tr} = \int_0^\infty (1+S-f'^2)d\eta \Big/ \int_0^\infty f'(1-f')d\eta \quad . \tag{68}$$

With the assumption of the applicability of Eq. (64) and (65), the right-hand side of the momentum integral equation (57) is a function only of β and S_w. Alternatively, β can be considered a function of n and S_w so that Eq. (57) is written in terms of a momentum parameter, N, in the form

$$-U_1 \frac{d}{dX}\left(\frac{m}{U_{1X}}\right) = N(n,S_w) \quad . \tag{69}$$

Solution of Eq. (69) for a given S_w will yield the pressure gradient parameter. The profile solutions of Reference 4 (given in terms of n and S_w) can then be consulted to obtain ℓ and H_{tr}.

Equation (69) is solved by assuming that the momentum parameter can be expressed by a linear equation in the form

$$N = A + Bn \quad , \tag{70}$$

where A and B are constants chosen from Reference 4 to give a good representation of N for each value of S_w. When Eq. (70) is substituted into Eq. (69) and the result transformed from X to x, the correlation number, n is given by

$$n = A\left(\frac{T_1}{T_o}\right)^{-(K+1)} \frac{M_1}{r_w^2}^{1-B} \frac{1}{u_1}\frac{du_1}{dx}\int_0^x \left(\frac{T_1}{T_o}\right)^K \frac{r_w^2}{M_1^{1-B}}\,dx + n_o \quad , \tag{71}$$

where $K = (3\gamma-1)/2(\gamma-1)$ and n_o is the value of n at $x = 0$.

With a prescribed set of free-stream flow properties, the correlation number n is computed from Eq. (71). The parameters H_{tr} and δ_{tr}/θ_{tr} are obtained from the tabulated profile solutions of Reference 4. The quantity δ_{tr} is defined as the value of η for which $f' = 0.995$. The local momentum thickness, displacement thickness, and physical thickness are calculated from the following relationships:

$$\theta_2 = \frac{T_1}{T_w} \left[\frac{\nu_w n}{du_1/dx} \frac{T_1}{T_o} \right]^{\frac{1}{2}} , \tag{72}$$

$$\delta_2^* = \theta_2 \left[H_{tr} + \frac{\gamma-1}{2} M_1^2 (H_{tr}+1) \right] , \quad \text{and} \tag{73}$$

$$\delta_2 = \theta_2 \left[\delta_{tr}/\theta_{tr} + \frac{\gamma-1}{2} M_1^2 (H_{tr}+1) \right] . \tag{74}$$

Solutions for the system of equations were obtained with an IBM 7094 digital computer. The computations were started in the subsonic flow at the nozzle entrance. The value of n_o was set equal to the value of n corresponding to a β of unity at the specified S_w. Equation (71) was then solved along the nozzle wall. No difficulty was encountered in passing through the throat. All derivatives were computed from the external Mach number and specified geometry with the formulas for the isentropic flow of a perfect gas with an arbitrary molecular weight and ratio of specific heats. The growth of the boundary layer was included in computation of area ratio derivatives.

An interative technique was employed to account for displacement interaction. The inviscid flow properties and boundary layer displacement thickness throughout the entire nozzle were computed and the displacement thickness obtained at each x-location was used to obtain the effective nozzle radius for the next iteration. At any given x-location, the effective nozzle radius for the i^{th} iterative solution was set equal to the geometric radius minus the average value of the displacement thicknesses calculated during the (i-1) and (i-2) iterations. The convergence of the technique is indicated in Fig. 2 where displacement thicknesses obtained from several iterations are shown. For the stagnation conditions of interest here, five iterations are required to obtain four-place accuracy in the displacement thickness. With the proper δ_2^* thus determined, Eq. (59) was solved to obtain the displacement thickness corrected for transverse curvature effects. No further iterations of the solution were performed.

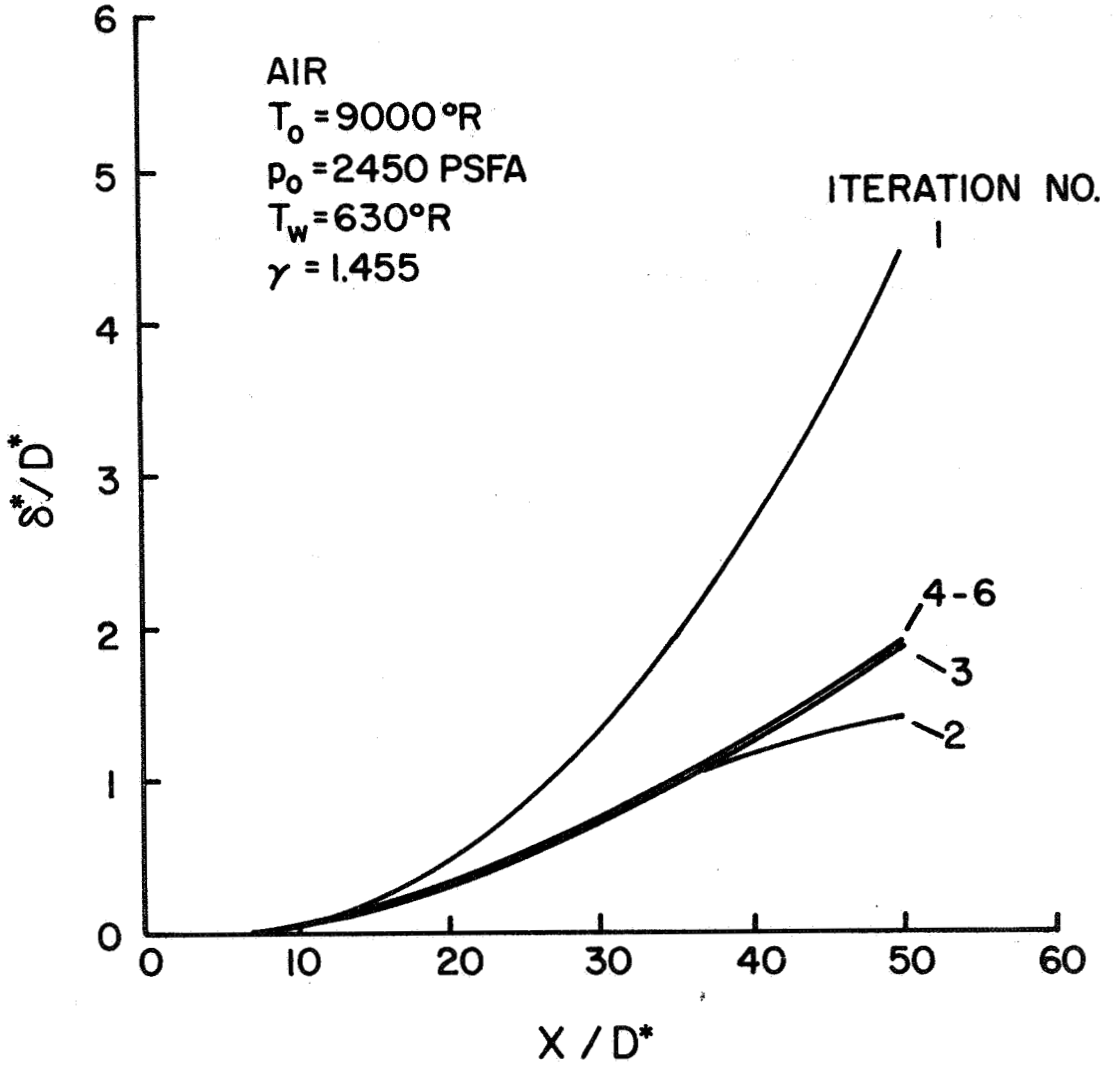

Fig. 2 - Convergence for Displacement Interaction by Method of Cohen and Reshotko

D. ALTERNATE TECHNIQUES OF ANALYSIS

1. Method of Beckwith and Cohen

The method of Cohen and Reshotko differs from that developed with the direct application of local similarity. With the usual application of local similarity, the pressure gradient parameter, β, is determined from Eq. (37) rather than from the correlation of N and n. The origin of each hypothetical flow which yields the local condition outside the boundary layer coincides with the origin of the physical flow. In the absence of displacement interaction, β depends only on the inviscid flow. However, in a nonsimilar flow the previous history of the boundary layer would also be expected to have some effect on the value of β.

Various attempts have been made to improve on the basic integral methods for computing boundary layer properties. Hayes and Probstein[15] propose a technique where an arbitrary scaling parameter $G(\xi)$ is introduced. The pressure gradient parameter and $G(\xi)$ are determined by simultaneous solution of momentum and energy integral equations in conjunction with similar solutions of the boundary layer equations to obtain profile parameters. While this technique removes the inconsistency in heat transfer calculations caused by neglect of the energy equation in the Cohen-Reshotko method, the influence of the prior history of the boundary layer is suppressed. In addition, the method is cumbersome to apply, particularly when displacement interaction effects must be included.

Beckwith and Cohen[5] propose a method for allowing prior history to influence the calculated boundary layer parameters. Local similarity in the boundary layer equations (28-33) is assumed but the origin of the similar flow is allowed to vary with the parameter ξ. The origin is determined by requiring that the energy integral equation be satisfied at every point along the wall. Hence, the previous history of the boundary layer enters in the definition of the pressure gradient parameter. Since the analysis was developed primarily to obtain heat transfer results, the energy integral equation, rather than the momentum integral equation, is employed.

The energy integral equation is obtained by neglecting transverse curvature (R=1) and integrating Eq. (29) from $\eta = 0$ to $\eta = \infty$. Setting the Prandtl number equal to unity and integrating gives

$$\frac{d}{d\xi}\left[\left\{2(\xi-\bar{\xi})^{\frac{1}{2}} S_w \Lambda_{tr}\right] = -\frac{1}{\sqrt{2(\xi-\bar{\xi})}} S'(0) \quad . \qquad (75)$$

The transformed convection thickness, Λ_{tr}, is defined as

$$\Lambda_{tr} = \int_0^\infty f'(1-\phi)\,d\eta \tag{76}$$

and

$$\phi = \frac{H-H_w}{H_1-H_w} = 1 - \frac{S}{S_w} \quad . \tag{77}$$

For a locally similar flow with $P_R = C = 1$, Eq. (28) and (29) become

$$\begin{aligned} f''' + ff'' + \beta(1+S-f'^2) &= 0 \\ S'' + fS' &= 0 \end{aligned} \tag{78}$$

It should be noted that Eq. (78) are exactly the same as Eq. (64) and (65) of the Cohen-Reshotko method so that the profile solutions from the two methods can be interchanged.

The energy integral equation for similar flow can be obtained either from Eq. (75) by setting all ξ -derivatives equal to zero, or from Eq. (78) by integrating on η from $\eta = 0$ to $\eta = \infty$. The result is

$$(g_\eta)_w = \left(1 - \frac{T_w}{T_o}\right)\Lambda_{tr} \quad . \tag{79}$$

The origin of the locally similar flow which describes the boundary layer at any stream-wise location is obtained by requiring that Eq. (79) hold at all points in the flow. Substituting Eq. (79) into Eq. (75) and integrating from $\xi = 0$ to $\xi = \xi$ gives the local origin $\bar{\xi}$ in the form

$$\xi = \bar{\xi} + \frac{1}{\Gamma^2}\left[\int_0^\xi \Gamma^2 d\xi - \bar{\xi}_o\right] \quad , \tag{80}$$

where

$$\Gamma = (g_\eta)_w / [(g_\eta)_w]_{REF} \quad . \tag{81}$$

and $[(g_\eta)_w]_{REF}$ is the wall enthalpy gradient at some reference point. With the ξ given by Eq. (80), the pressure gradient parameter, β, can be determined. Thus

$$\beta = \frac{2(\xi-\bar{\xi})}{U_1} U_{1\xi} = \frac{2}{U_1}\frac{U_{1\xi}}{\Gamma^2}\left[\int_0^\xi \Gamma^2 d\xi - \bar{\xi}_o\right] \quad . \tag{82}$$

Transforming Eq. (82) to the (x.y) plane gives

$$\beta = \frac{\frac{2}{u_1^2}\frac{T_o}{T_1}\frac{du_1}{dx}}{\rho_w \mu_w r_w^2 \Gamma^2} \int_0^x \rho_w \mu_w u_1 r_w^2 \Gamma^2 dx + \beta_o \quad . \tag{83}$$

The pressure gradient parameter is obtained by solution of Eq. (83). However, the heat transfer function Γ is determined from solution of the similarity form of the profile equations which depend on β. Hence, an iterative method of solution must be used to obtain β.

The need for iteration in the determination of β can be eliminated with an approximation to the method of Beckwith and Cohen. An empirical form for ϕ'_w developed in Reference (5) is

$$\frac{\phi'_w}{\phi'_{w_1\beta=1}} \quad \frac{1 + P\beta^N}{Q + R\beta^N} \quad . \tag{84}$$

The parameters P, Q, R, and N are functions of T_w and T_o evaluated by fitting Eq. (84) to the results of the similar profile solutions. For $\beta \geq \frac{1}{2}$, Eq. (84) agrees with the profile solutions within approximately 0.5 per cent.[5]

For an isothermal wall, the heat transfer function is given by

$$\Gamma = \frac{\phi'_w}{\phi'_{w,REF}} = \frac{\phi'_w}{\phi'_{w,\beta=1}} \frac{\phi'_{w,\beta=1}}{\phi'_{w,REF}} \quad . \tag{85}$$

With Eq. (83-85), a differential equation for β can be developed as

$$\frac{d\beta}{dx} = \frac{p_1 u_1 r_w^2 - (\beta-1)dE/dx}{E\left[1 + \frac{2}{F}\frac{dF}{d\beta}(\beta-1)\right]} \quad , \tag{86}$$

where

$$E = \frac{T_1}{T_o}\frac{u_1^2}{2}\frac{p_1 r_w^2}{du_1/dx} \quad , \tag{87}$$

$$F = \frac{1 + P\beta^N}{Q + R\beta^N} \quad , \tag{88}$$

and β_o is set equal to unity for nozzle flows.

Equation (86) is in a form which can easily be integrated with a digital computer to obtain β. With β and a given T_w/T_o, the tabulated profile solution can be consulted to obtain the boundary layer parameters of interest. Since the profile solutions are identical to those of the Cohen-Reshotko method, the computing scheme described in the previous section can be employed here.

The local values of β were obtained by solving Eq. (86). The value of the correlation number, n, and the profile parameters, H_{tr} and ℓ, were obtained from the profile solutions. The local momentum thickness, displacement thickness, and physical thickness were calculated from Eq. (72-74).

The iteration technique to account for displacement interaction was exactly the same as that described in the previous section. It is to be noted that in nozzle flows the Beckwith-Cohen and Cohen-Reshotko methods differ only in the manner in which the pressure gradient parameter is determined.

2. Pohlhausen Methods

In the application of the Pohlhausen technique, assumed velocity and enthalpy profiles are used in the solution of either the momentum integral equation or the energy integral equation. Since transverse curvature effects can be included directly with these methods, they were examined for possible application to high-enthalpy nozzle flows. Luce, Gregorek, and Lee[3] report some success with the Pohlhausen momentum integral method for low-enthalpy nozzle flows.

The velocity and enthalpy profiles are assumed to be given by fourth-order polynomials in the transformed y-direction. That is, let

$$\frac{u}{u_1} = \sum_{i=0}^{4} a_i(x)\eta^i \tag{89}$$

and

$$\varphi = \sum_{i=0}^{4} b_i(x)\eta^i \quad , \tag{90}$$

where the transformation from y to η is given by

$$\eta = \frac{1}{\Delta}\int_0^y \frac{\rho}{\rho_1}\, dy \tag{91}$$

and Δ is the transformed boundary layer thickness. The physical thickness, δ, is given in terms of Δ by

$$\delta = \Delta\int_0^1 \frac{T}{T_1} d\eta \quad . \tag{92}$$

Application of boundary conditions at the wall and at the outer edge of boundary layer ($y = \delta$) gives[3]

$$\frac{u}{u_1} = \frac{3}{3+\beta}\left[(2\eta-2\eta^3+\eta^4) + \frac{\beta}{3}(6\eta^2-8\eta^3+3\eta^4) + \frac{\lambda}{6}(\eta-3\eta^2+3\eta^3-\eta^4)\right] \quad (93)$$

and

$$\varphi = \frac{3}{3+\beta}\left[(2\eta-3\eta^3+\eta^4) + \frac{\beta}{3}(6\eta^2-8\eta^3+3\eta^4)\right] , \quad (94)$$

where

$$\beta = \frac{\Delta}{2r_w}\frac{\rho_1}{\rho_w}\cos\alpha ,$$

$$\lambda = \frac{\Delta^2\rho_1^3}{\mu_w\rho_w^2}\frac{du_1}{dx} = \left(\frac{2\beta r_w}{\cos\alpha}\right)^2\frac{\rho_1}{\rho_w}\frac{du_1}{dx} , \quad \text{and} \quad (95)$$

$$\Delta = 2\frac{r_w\beta}{\cos\alpha}\frac{T_1}{T_w}$$

With the velocity and enthalpy profiles given by Eq. (93) and (94), the pertinent boundary layer parameters can be determined in terms of λ and β; e.g.,

$$\frac{\delta}{\Delta} = \frac{H_w}{h_1} + \frac{H_1}{h_1}\left(1-\frac{h_w}{h_1}\right)\sum_j\frac{b_j}{j+1} - \frac{\gamma-1}{2}M_1^2\sum_{i,j}\frac{a_i a_j}{i+j+1} . \quad (96)$$

Similar relationships can be given for the displacement thickness defined by Eq. (25), the momentum thickness defined by Eq. (24), and the energy thickness defined by

$$\delta_H = \int_0^\infty\left(1-\frac{H}{H_1}\right)\frac{\rho u}{\rho_1 u_1}\frac{r}{r_w}\,dy . \quad (97)$$

The boundary layer parameters were obtained with an iterative solution employing either the momentum integral equation in the form

$$\frac{d\theta}{dx} + \frac{\theta}{\rho_1 u_1^2 r_w}\frac{d}{dx}(\rho_1 u_1^2 r_w) + \frac{\delta^*}{u_1}\frac{du_1}{dx} = \frac{C_f}{2} , \quad (98)$$

or the energy integral equation

$$\frac{d\delta_H}{dx} + \frac{\delta_H}{\rho_1 u_1 r_w} \frac{d}{dx} (\rho_1 u_1 r_w) = - q_w/\rho_1 u_1 H_1 \quad . \tag{99}$$

At any given x-location in the nozzle, the value of β was estimated from that obtained at the previous step. With specified free-stream conditions, λ and Δ could then be computed from Eq. (95). The momentum thickness, θ; displacement thickness, δ^*; and convection thickness, δ_H, were calculated from equations similar to Eq. (96). In the momentum integral solution, the value of β was then adjusted until the θ obtained from the assumed β agreed with that resulting from the solution of Eq. (98). Similarly, in the energy integral solution, adjustment of β was accomplished by solving Eq. (99) for δ_H.

Two techniques for including displacement interaction were employed. The first technique was that described in the previous section. The alternate technique consisted of adjusting the effective nozzle radius at each x-location and reiterating to obtain the correct value of β. Thus, the entire solution, including curvature and interaction effects, was obtained in a single integration through the nozzle.

E. BOUNDARY LAYER PROFILES

To evaluate the influence of transverse curvature and to allow comparisons of the experimental data with results from the various similarity methods, boundary layer profiles were obtained from solutions of Eq. (43-46), repeated below for convenience:

$$(Rf'')' + ff'' + \beta(1+S-f'^2) = 0 \tag{43}$$

$$(RS')' + P_R f S' + \frac{u_1^2}{H_1}(P_R-1)(Rf'f'')' = 0 \tag{44}$$

$$R = 1 - A_1 \int_0^\eta \frac{T}{T_1} \, d\eta \tag{45}$$

$$\frac{T}{T_1} = f'^2 + \frac{H_1}{h_1} (1+S-f'^2) \quad . \tag{46}$$

where A_1 is given by Eq. (39).

The equations were solved for given free-stream flow properties and values of β obtained from the various similarity analyses. Solutions were obtained both with and without the transverse curvature terms. An iterative technique was used to obtain the solutions.

Initial values of $S(\eta)$ and $R(\eta)$ were assumed and Eq. (43) was solved for $f(\eta)$. The assumed $R(\eta)$ and the $f(\eta)$ distributions were used in the first solution of Eq. (44). With this corrected distribution of $S(\eta)$, Eq. (45) was solved for $R(\eta)$. Consecutive solutions for $S(\eta)$ and $R(\eta)$ were performed until the solution for $S(\eta)$ converged. The solutions for R and S were then used to obtain a corrected solution for Eq. (43) and the entire iteration procedure was repeated. The computations were terminated when the value of $f''(0)$ converged within a specified error criterion.

The transformation from η to y is required to compare the experimental and theoretical profiles. When transverse curvature is included, this transformation is given by

$$y = \frac{r_w}{\cos \alpha} \left[1-\left(1-2\frac{\cos \alpha}{r_w} y_2\right)^{\frac{1}{2}}\right] \quad , \tag{100}$$

where y_2 is the corresponding y-value when transverse curvature effects are neglected. Thus,

$$y_2 = c(x)\int_0^{\eta} \frac{\rho_1}{\rho} \, d\eta \quad , \tag{101}$$

with $c(x)$ given by Eq. (60). The parameter A_1 in Eq. (45) is related to $c(x)$ by

$$A_1 = \frac{2 \cos \alpha}{r_w^2} c(x) \quad . \tag{102}$$

To compare profiles from the various methods, $c(x)$ was adjusted so that each profile solution gave the correct physical boundary layer thickness. That is, before the η to y transformation was performed, $c(x)$ was obtained from

$$c(x) = \delta / \int_0^{\eta_\infty} \frac{\rho_1}{\rho} \, d\eta \quad , \tag{103}$$

where η_∞ corresponds to a velocity ratio u/u_1 of 0.995 and δ is the experimental boundary layer thickness. When curvature effects were included, the differences between y and y_2 were ignored and $c(x)$ was determined from a solution neglecting curvature. The value of A_1 was then computed from Eq. (102) and the profile solutions with curvature were obtained.

The main reason for obtaining these profile solutions was to test the ability of each technique to give adequate boundary layer profiles. The scaling of y separates the boundary layer thickness determination from the solutions for detailed profiles.

In addition to the similarity profiles, velocity and enthalpy profiles resulting from the asymptotic solution of Coles[17] were generated for comparison with the experimental data. From Reference 17, the asymptotic solutions for velocity and enthalpy can be written as

$$\frac{u}{u_1} = \left[1 + S_w \mathrm{ERFC} \left\{ \left[\frac{(1+S_w)^{3/2}-1}{S_w} \right]^{\frac{1}{2}} \frac{\eta}{\sqrt{3}} \right\} \right]^{\frac{1}{2}} + \left[-3(1+S_w)^{\frac{1}{2}} \mathrm{SECH}^2 \left[(1+S_w)^{\frac{1}{4}} \sqrt{\beta/2}\, \eta + \mathrm{TANH}^{-1} \sqrt{\frac{2}{3}} \right] \right] + O\left(\frac{1}{\sqrt{\beta}}\right) \tag{104}$$

and

$$S = S_w \mathrm{ERFC} \left\{ \frac{\eta}{\sqrt{3}} \left[\frac{(1+S_w)^{3/2}-1}{S_w} \right]^{\frac{1}{2}} \right\} + O\left(\frac{1}{\sqrt{\beta}}\right) . \tag{105}$$

A β of 20 was chosen to generate the asymptotic profiles. The scaling of y to give the correct boundary layer thickness discussed above also was employed with Eq. (104) and (105).

III. EXPERIMENTAL APPARATUS AND PROCEDURES

A. WIND TUNNEL FACILITY

The experimental studies were conducted in the OSU arc-heated wind tunnel. The facility consists of a direct-current arc heater, a settling chamber, a conical nozzle, a free-jet test cabin, and a pressure recovery system. The heater was operated with air and provided stagnation enthalpies from 2000 to 6000 Btu/lb at stagnation pressures near 1 atmosphere. The usual run time for the facility in these studies was two hours, allowing the use of conventional wind tunnel instrumentation.

Boundary layer profiles were obtained with an electron beam and various probes described in the following sections. The electron beam was projected through the nozzle wall and data were obtained from the length of beam immediately outside of the exit orifice of the beam generating system. Since the nozzles were water cooled, insertion of a window to allow observation of the beam would have presented extreme mechanical difficulties. Instead, the beam was passed through the nozzle a small distance upstream of the nozzle exit. The optical system, shown schematically in Fig. 3, viewed the beam from an oblique

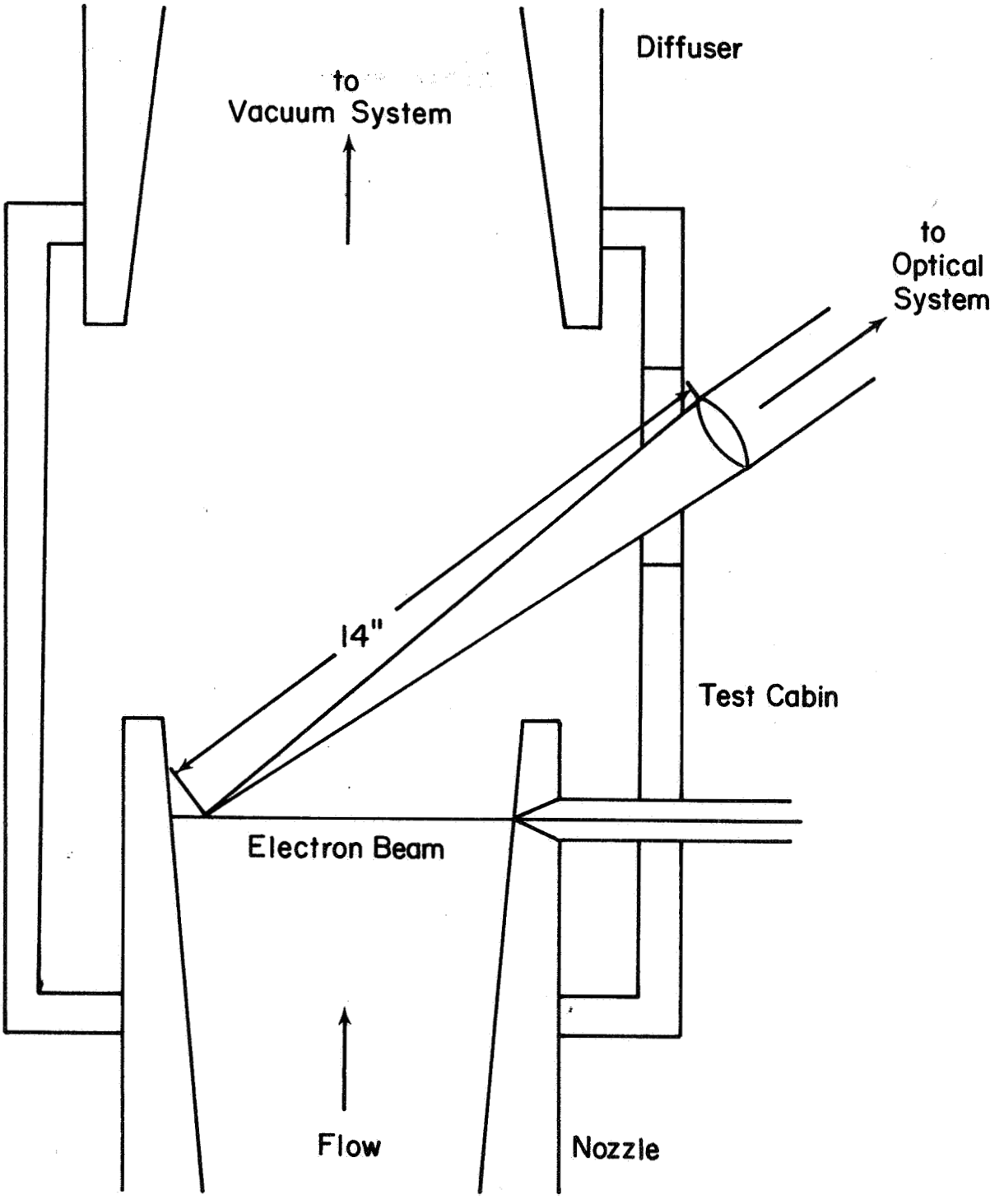

Fig. 3 - Wind Tunnel Schematic

angle. Boundary layer profiles at the various axial stations were obtained by testing three separate nozzles. The nozzle geometry and nomenclature employed are shown in Fig. 4. The locations of stations 3 and 4 were chosen to maintain a minimum distance from the point of observation to the nozzle exit equal to three boundary layer thicknesses.

B. ELECTRON BEAM INSTRUMENTATION

With the electron beam, the rotational temperature, vibrational temperature, and concentration of molecular nitrogen can be measured at arbitrary locations within the flow. Since the rate of equilibration of the rotational and translational degrees of freedom is extremely rapid, a rotational temperature measurement gives an accurate measurement of the static temperature of the gas. The rotational temperatures were obtained from analysis of the $N_2^+(0,0)$ band at 3914 Å. The nitrogen vibrational temperatures were determined by measuring the relative intensities of the $N_2^+(0,1)$, (1,2), and (2,3) vibrational bands. The techniques of data interpretation have been described adequately elsewhere[9,18,19] and will not be discussed here. The electron beam was generated with an energy near 15 keV and beam currents near 500 μA. The beam diameter was approximately 2 mm. Spectral resolution of the measurements was accomplished with a Jarrell-Ash 0.5-meter Ebert scanning spectrometer. The optical system used with the spectrometer is shown schematically in Fig. 5.

When an electron beam is passed through a partially ionized flow, thermal electrons trapped in a potential well centered around the beam contribute to the measured beam current. This contribution has caused large fluctuations in the observed beam current and can lead to uncertainties in temperature determinations. To circumvent the effects of fluctuating beam currents, the reference photomultiplier shown in Fig. 5 was employed. The reference photomulitplier was fitted with a narrow band-pass filter with a half-width of approximately 100 Å and a center of peak transmission near 3900 Å. The radiation from the electron beam was collimated by lens (2) (see Fig. 5) and passed through a 70-30 splitter. The major portion of the radiation was re-focused by lens (1) and passed into the spectrometer. The remainder of the light was focused by lens (3) through the filter onto the cathode of the reference photomultiplier. An uncooled EMI 9502S photomultiplier was employed with the spectrometer.

The photo-currents were measured and amplified with Keithley model 417(K1) and 410(K2) pico-ammeters. The outputs from the pico-ammeters entered an on-line analog computer where the ratio of the EMI and reference photomultiplier outputs was formed. The ratio was plotted versus wavelength on a X-Y plotter. Since both the EMI and reference photomultiplier outputs varied linearly with beam current, the resulting ratio of the two signals was independent of beam current. Hence, the effects of changes in beam current during the course of a wavelength scan were automatically removed from the final recorded signals.

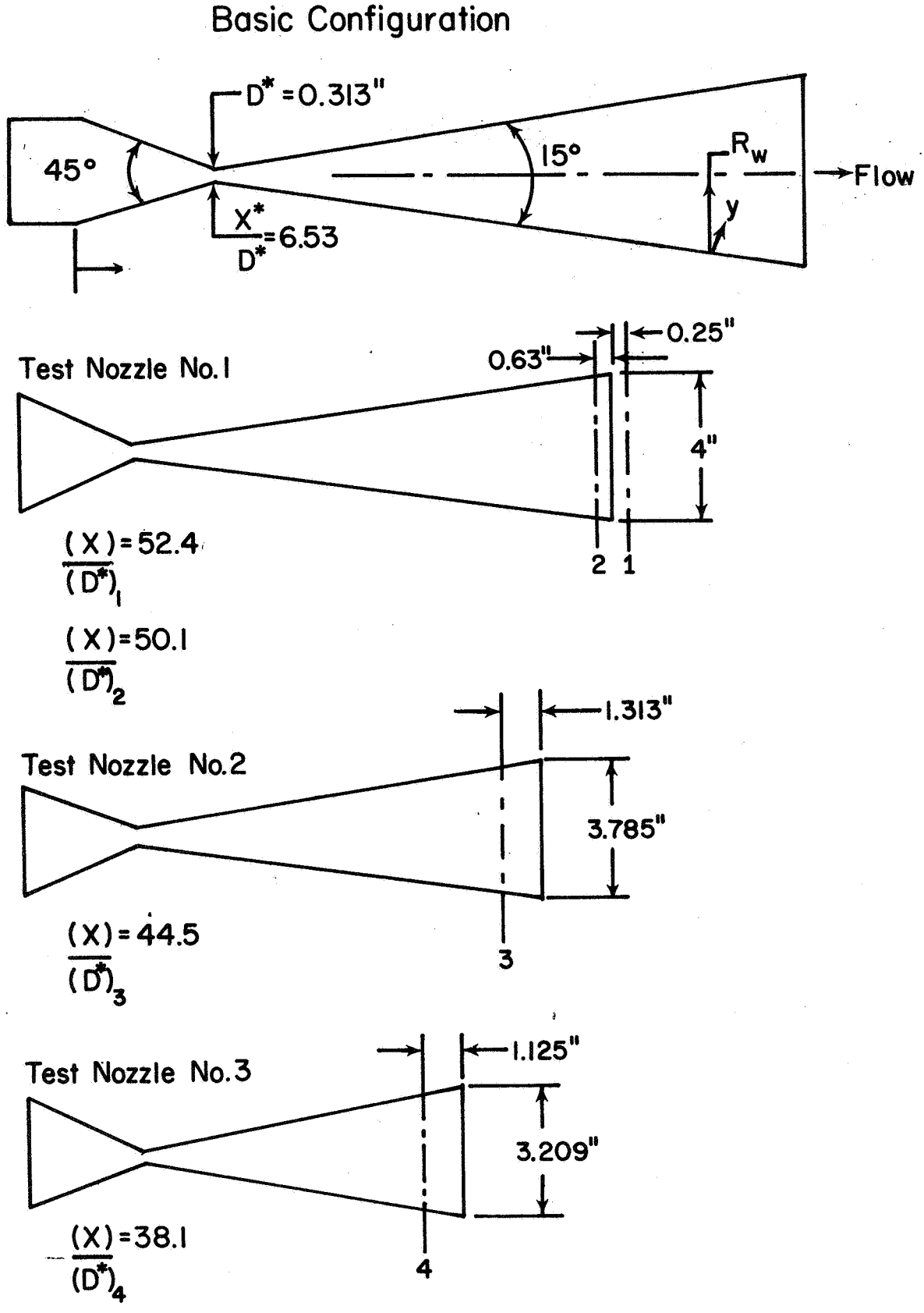

Fig. 4 - Nozzle Geometry

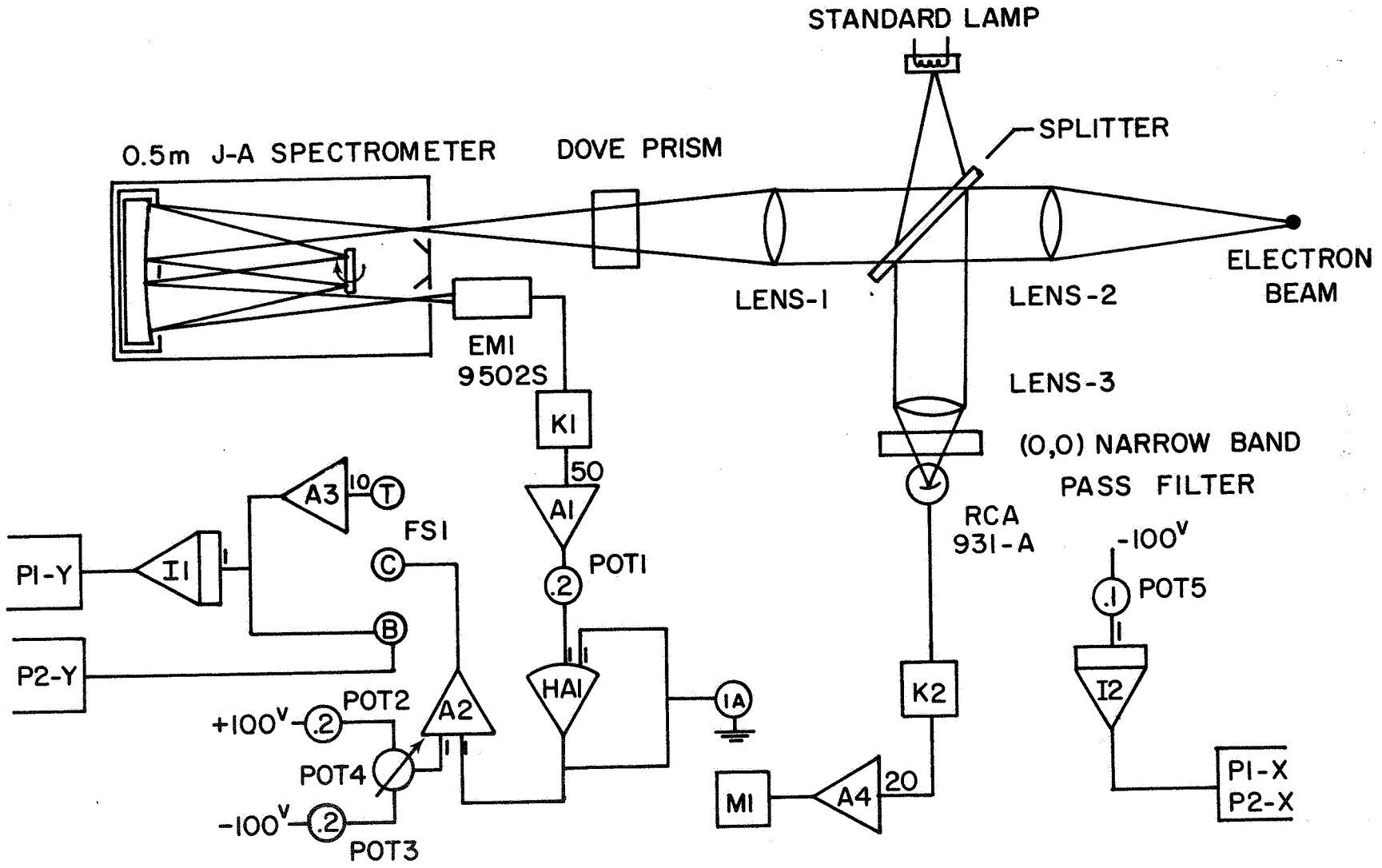

Fig. 5 - Optical System Schematic

The image of the electron beam was rotated through 90° by the dove prism so that the entrance slit and beam image were perpendicular. With this arrangement, the spatial resolution of the measurements in the direction along the length of the beam (perpendicular to the nozzle wall) was better than 0.003 inch. Since the boundary layer thickness was near one inch, this spatial resolution allowed detailed boundary layer profiles to be obtained. The spectrometer and optics were mounted on a traversing table so that data could be obtained from arbitrary positions along the length of the electron beam.

For the rotational temperature measurements, the spectrometer entrance and exit slit widths were set at 0.030 mm. This value was chosen so that rotational lines in the $N_2^+(0,0)$ band with rotational quantum numbers greater than 3 were resolved. The time constants of the two photomultiplier circuits were adjusted to minimize the electrical noise without severly limiting the time response of the system. Rotational temperatures were obtained with a scan speed of 5 Å/min. A typical profile of the $N_2^+(0,0)$ band obtained with the ratio of the two photomultiplier signals is shown in Fig. 6.

For vibrational temperature measurement, the slit widths of the spectrometer were set at 0.100 mm and the ratio of the signals was integrated by the analog computer. The absolute outputs from each photomultiplier as well as the integration of the ratio of signals were displayed on X-Y plotters so that the effects of integrated noise could be examined. Typical output records are shown in Fig. 7. Band profiles obtained both at room temperature and with an elevated vibrational temperature are shown in Fig. 7 to illustrate the influence of vibrational temperature on the intensity distributions. The increase in relative intensity of the bands resulting from emission from upper vibrational energy levels at high vibrational temperature is evident in Fig. 7.

Since only bands in the (0,1) progression were employed for vibrational temperature determination, no corrections for the spectral response of the optical system were applied. With the arrangement shown in Fig. 5, rotational and vibrational temperature could be obtained with accuracies better than ± 3% and ± 10%, respectively.

A limited number of measurements of nitrogen concentration within the boundary layer were made with the electron beam. The density determination is based upon the linear dependence of the intensity of the beam-induced radiation with molecular nitrogen concentration. However, the intensity of the observed radiation also varies linearly with the beam current. The large random fluctuations of the beam current discussed above made accurate density determinations with the spectrometer extremely difficult.

The density profiles within the boundary layer were obtained with a spectrograph recording the intensities on Kodak type 103a-0 spectroscopic plates. A Baird 3-meter grating spectrograph was employed for

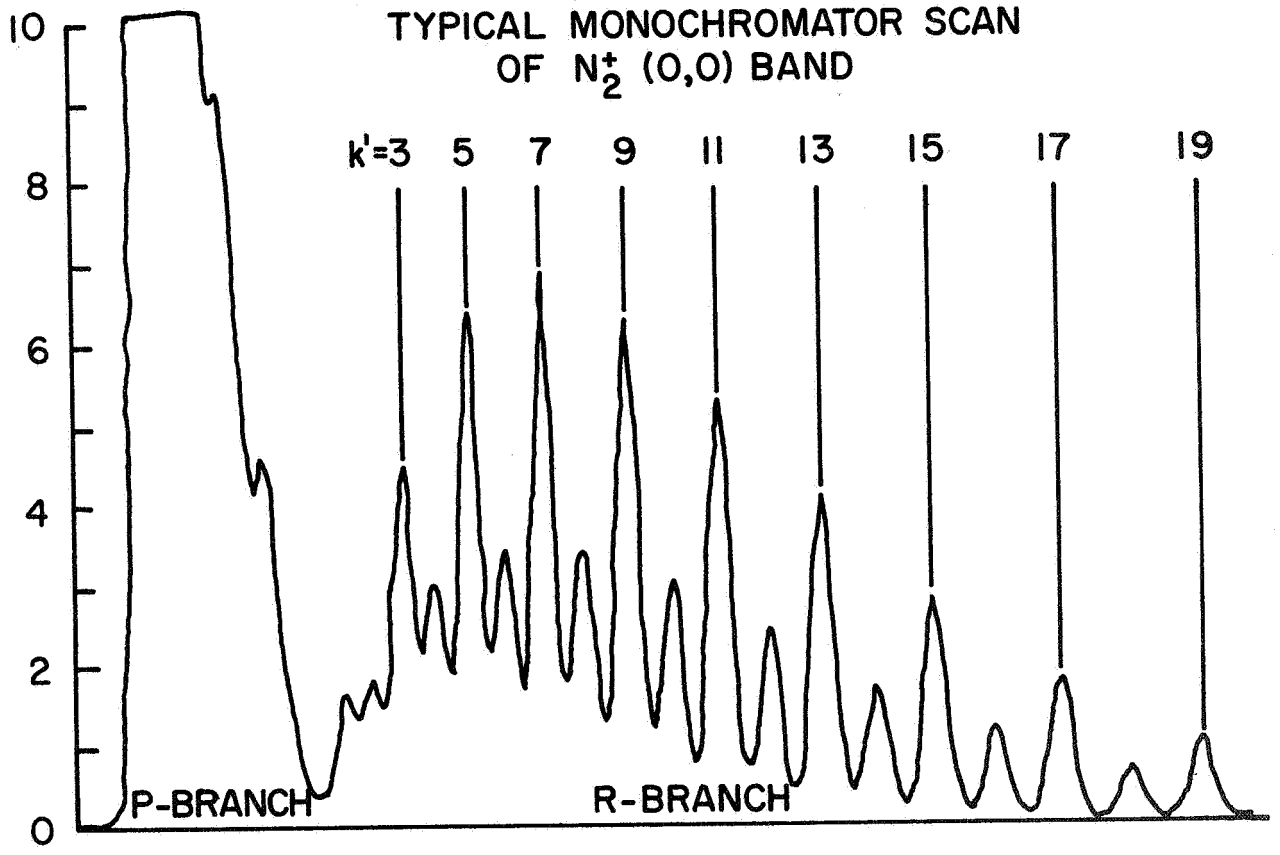

Fig. 6 - Rotational Line Survey

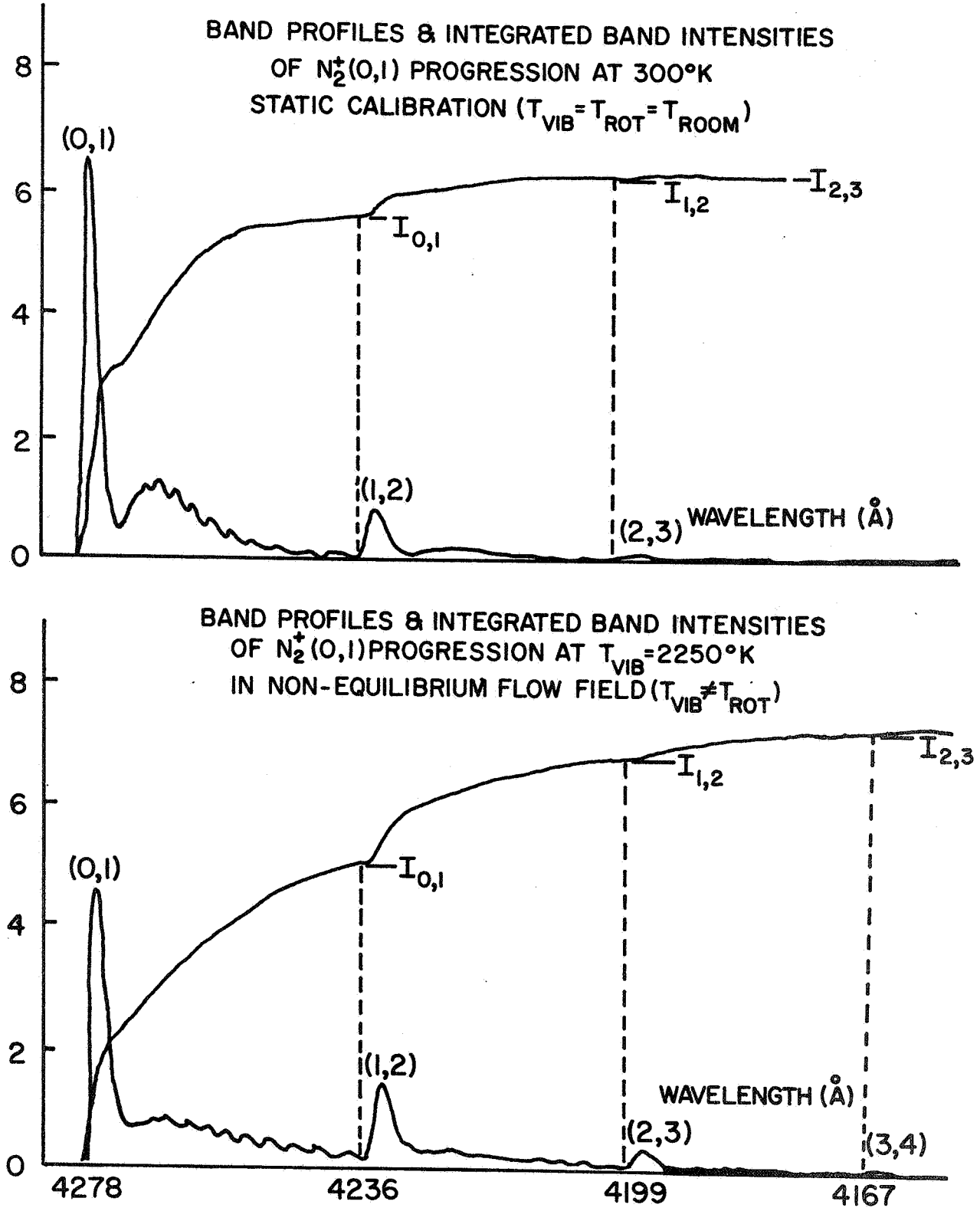

Fig. 7 - Vibrational Band Surveys

the density measurements and a limited number of rotational and vibrational temperature measurements. With a reciprocal linear dispersion of 5.6 Å/mm and a slit width of 0.100 mm, the instrument has sufficient resolution to separate the rotational lines within the $N_2^+(0,0)$ band.

Each spectroscopic plate was calibrated to determine the relationship between radiation intensity and the photographic density. A National Spectrographic Laboratories recording microdensitometer was employed for data reduction. An exposure time of approximately 20 minutes was required to obtain optimum photographic density.

The slit of the spectrograph was aligned with the electron beam. The beam-induced radiation was focused at the stigmatic point of the spectrograph so that each point along a spectral line corresponded to a particular location along the length of the beam. Density profiles thus were obtained from the intensity distribution along the spectral lines. A reference mark to indicate the precise location of the nozzle centerline was placed on each plate and the magnification of the optics was determined experimentally. The full height of the spectral image corresponded to approximately three inches in the flow. The spatial resolution of these measurements was limited to 0.1 inch along the length of the beam because of the slit width of the micro-densitometer.

Since all points along the spectral image respond identically to fluctuations in the beam current, the nondimensional density profile will not be affected by beam current changes. The density profiles were obtained from the intensity distributions of several rotational lines. The line intensity variations through the boundary layer were corrected for both rotational and vibrational temperature variations by the method given in Reference 18. Since accurate alignment of the spectrograph slit with the beam is required in this technique, density measurements were made only in the free-jet (nozzle station No. 1) where the alignment of the beam and slit could be checked during each wind-tunnel run.

C. PROBES

In addition to the electron beam, various boundary layer profiles were obtained with mass-flow and pitot pressure probes. The mass-flow probe was connected to a vacuum system so that the shock wave system at the probe tip was "swallowed" by the probe. While it is customary to assume that the probe inlet and capture areas are equal in this configuration, the low Reynolds number nature of the flow introduces uncertainties in the effective probe inlet area. For this reason, the probe was calibrated in a perfect-gas wind tunnel. The probe inlet Reynolds number expected in the arc-tunnel flow was duplicated in the perfect-gas facility and the effective inlet area determined.

The mass-flow rate per unit area was obtained with a calibrated orifice. The instrumentation system is shown schematically in Fig. 8.

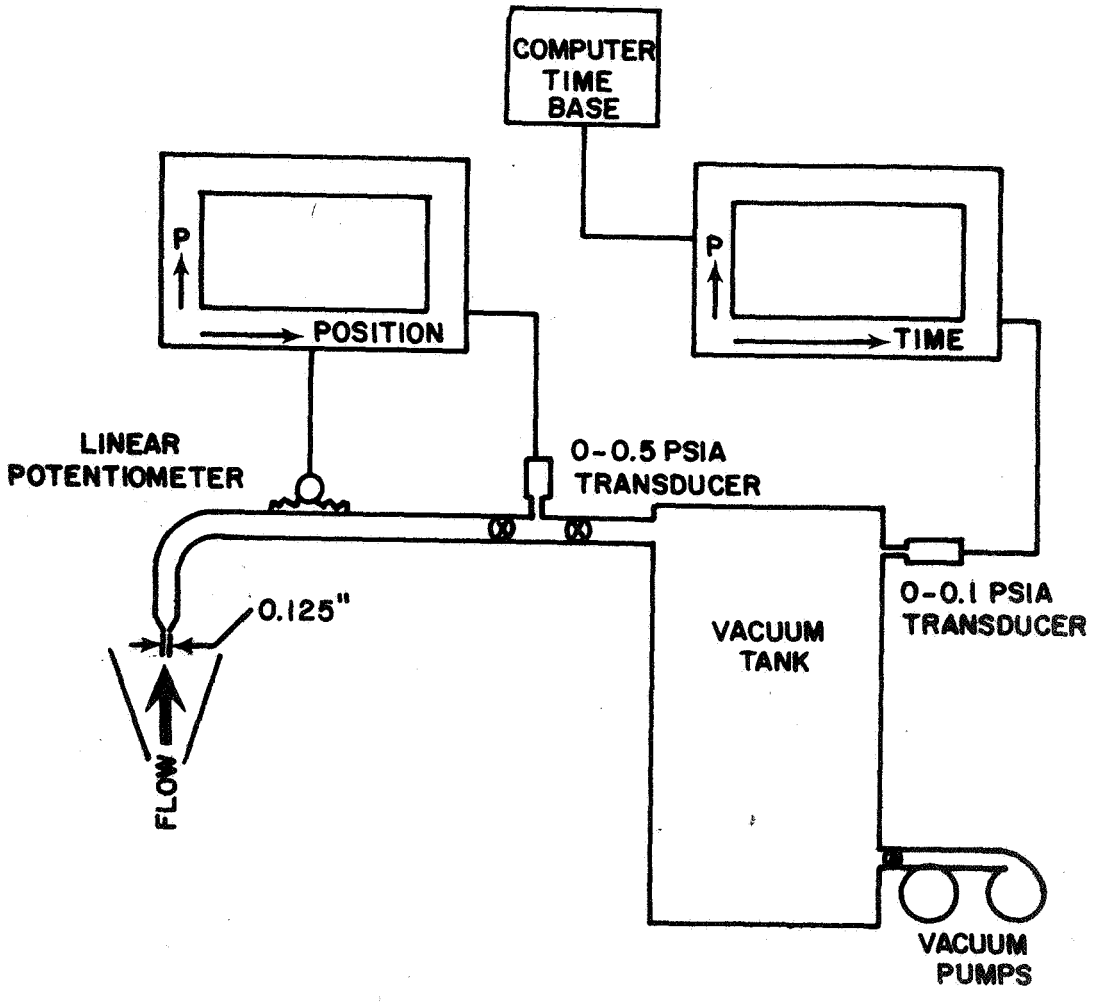

Fig. 8 - Probe Schematic

The pressure upstream of the orifice was measured with a variable reluctance pressure transducer. The transducer output was calibrated versus mass-flow rate during each wind-tunnel run by measuring the mass flowing through the probe with a bleed-up tank at several locations within the boundary layer. The bleed-up tank was then connected directly to the probe vacuum pumps and a continuous scan of mass flow rate per unit area was obtained with the pressure transducer and a position potentiometer. The on-line analog computer was used to convert the transducer and potentiometer outputs to corrected pressure and position; the profiles were recorded on a X-Y plotter. With the valve to the bleed-up tank and vacuum pumps closed, the probe recorded pitot pressure. Typical wind-tunnel records of pitot pressure and mass flow per unit area are given in Fig. 9.

The external diameter of the probe inlet was 0.125 inch. The probe tip had sharp lips and was internally chambered to minimize the effect of the low Reynolds number on measured pitot pressures.

D. DATA ANALYSIS

Boundary layer profiles were obtained by combining the data obtained from the electron beam and the probes. The static temperature ratio, T/T_1, was obtained directly with the electron beam while the pitot pressure ratio, pT_2/pT_1, and mass flow ratio, $\rho u/\rho_1 u_1$, were measured with the probe. The pitot pressure ratio was assumed equal to $\rho u^2/\rho_1 u_1^2$. The various profiles were obtained as indicated below.

$$\frac{u}{u_1} = \frac{pT_2}{pT_{2_1}} \Big/ \frac{\rho u}{\rho_1 u_1}$$

$$= \left[\frac{pT_2}{pT_{2_1}} \Big/ \frac{T}{T_1} \right]^{\frac{1}{2}} , \tag{106}$$

$$\frac{\rho u}{\rho_1 u_1} = \frac{pT_2}{pT_{2_1}} \Big/ \left(\frac{T}{T_1} \right)^2 ,$$

and

$$\frac{\rho}{\rho_1} = \frac{\rho u}{\rho_1 u_1} \Big/ \frac{u}{u_1} = 1 \Big/ \frac{T}{T_1} .$$

The properties of the inviscid flow at the outer edge of the boundary layer were obtained by assuming that complete chemical and vibrational freezing occurred at the nozzle throat. With the measurement of tunnel mass-flow rate and stagnation pressure, the stagnation enthalpy was obtained by assuming an equilibrium (chemical and thermodynamic) expansion from the settling chamber to the nozzle throat.

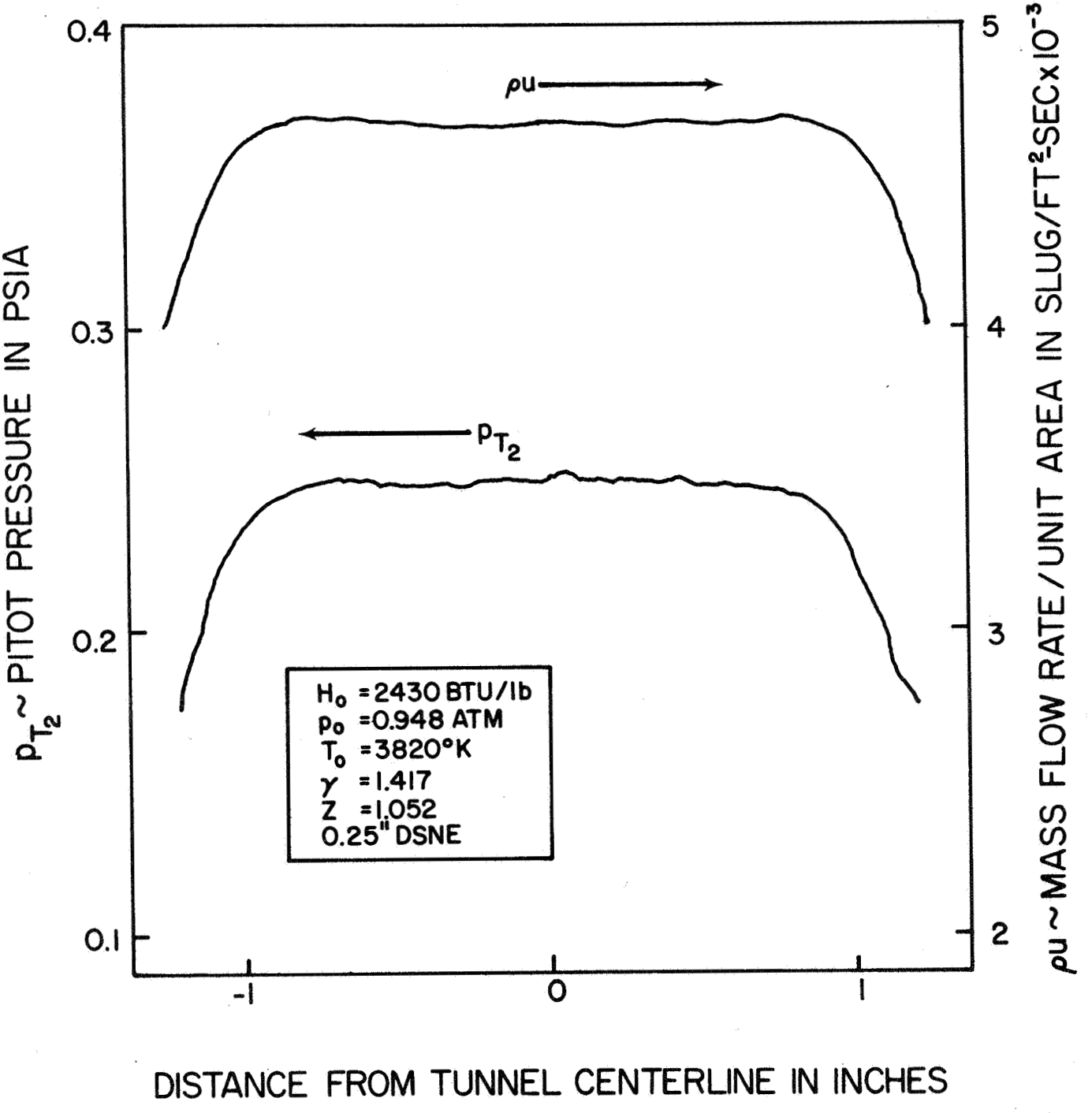

Fig. 9 - Typical Pitot and Mass Flow Profiles

The gas properties in the supersonic portion of the flow were obtained from the usual isentropic flow relations with a ratio of specific heats and molecular weight equal to those at the throat. With known stagnation conditions, measurement of local pitot pressure was sufficient to define all flow variables at the outer edge of the boundary layer. The mass-flow probe and electron beam data obtained in the high-speed core were employed to obtain flow density, velocity, and static temperature, and the results were compared with the values inferred from the pitot pressure measurement.

Typical comparisons of the theoretical and experimental flow properties are given in Fig. 10. The flow density, velocity, and static temperature resulting from assuming complete chemical and thermodynamic equilibrium in the expansion are included in Fig. 10 to illustrate the influences of flow chemistry on the inviscid flow properties. The chemical composition of the gas corresponding to the data of Fig. 10 is listed in Table I. It is to be noted that oxygen dissociation was nearly complete in the flow and that little nitrogen dissociation occurred.

Table 1 - Species Concentrations at T_o = 4600°K, P_o - 1.2 atm

Species	Concentration Moles/Mole of Mixture
N_2	0.5561
O_2	0.0059
AR	0.0683
N	0.0741
O	0.2712
NO	0.0244

The agreement between the measured inviscid flow properties and those computed with the frozen flow model is typically ± 6%, substantiating the applicability of the theoretical method.

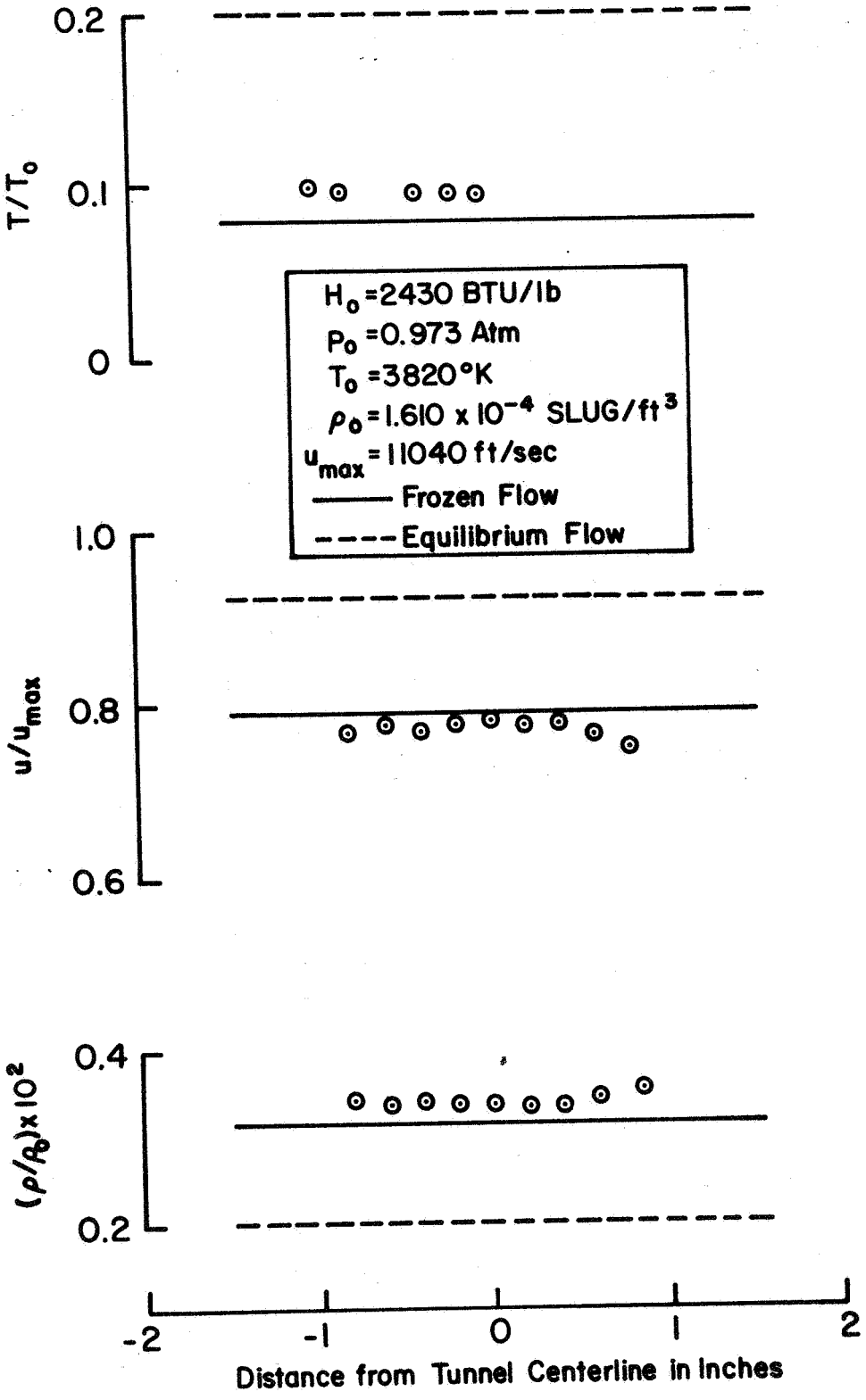

Fig. 10 - Inviscid Flow Properties

IV. RESULTS AND DISCUSSION

A. BOUNDARY LAYER THICKNESSES

Pitot pressure surveys in the boundary layer at the four test locations are shown in Fig. 11. It is to be noted that the nondimensional pitot pressure profiles at stations 3 and 4 are nearly identical. This demonstrates that the profiles obtained at these stations are free from distrubances caused by slight pressure differences between the nozzle-exit static pressure and the pressure in the wind-tunnel test cabin. The effects of these pressure unbalances can be seen clearly in the pitot pressure profiles obtained in the near vicinity of the nozzle exit at stations 1 and 2.

Typical comparisons of the theoretical and measured boundary layer thicknesses are shown in Fig. 12. The experimental displacement thicknesses were determined from the effective inviscid area ratio obtained from the measured pitot pressure and the frozen flow model for the nozzle expansion process. The physical boundary layer thickness was defined as the distance from the nozzle wall to the local maximum in pitot pressure at the outer edge of the boundary layer.

It is evident in Fig. 12 that the Pohlhausen techniques employing both the energy integral equation and the momentum integral equation are unsatisfactory. The failure of the Pohlhausen methods to give adequate boundary layer thicknesses is related to the allowable range for the pressure gradient parameter, λ, defined by Eq. (95). In the usual Pohlhausen method with no transverse curvature, an infinite pressure gradient corresponds to a λ of 12.[20] When curvature effects are included, the value of λ for infinite pressure gradient depends on the value of β (Eq. 103) but does not vary appreciably from 12.

For perfect gas flow through a nozzle, λ can be given by

$$\lambda = f(A/A^*)\Delta^2\sqrt{T_o} \quad , \tag{107}$$

where Δ is the transformed boundary layer thickness and $f(A/A^*)$ depends only on the nozzle geometry. Hence, large pressure gradient parameters result from large boundary layer thicknesses and high stagnation temperatures. In these studies values of λ greater than 12 were obtained at low supersonic Mach numbers. Hence, the Pohlhausen methods are not applicable in high-enthalpy flows with stagnation conditions in the range investigated.

The differences between the Beckwith-Cohen and Cohen-Reshotko boundary layer thicknesses shown in Fig. 12 are due solely to differences in the pressure gradient parameter, β, resulting from each technique. In these integral methods only one of the integral equations, either the energy integral or momentum integral equation, is used to determine β. When heat transfer data are of most interest, the energy integral

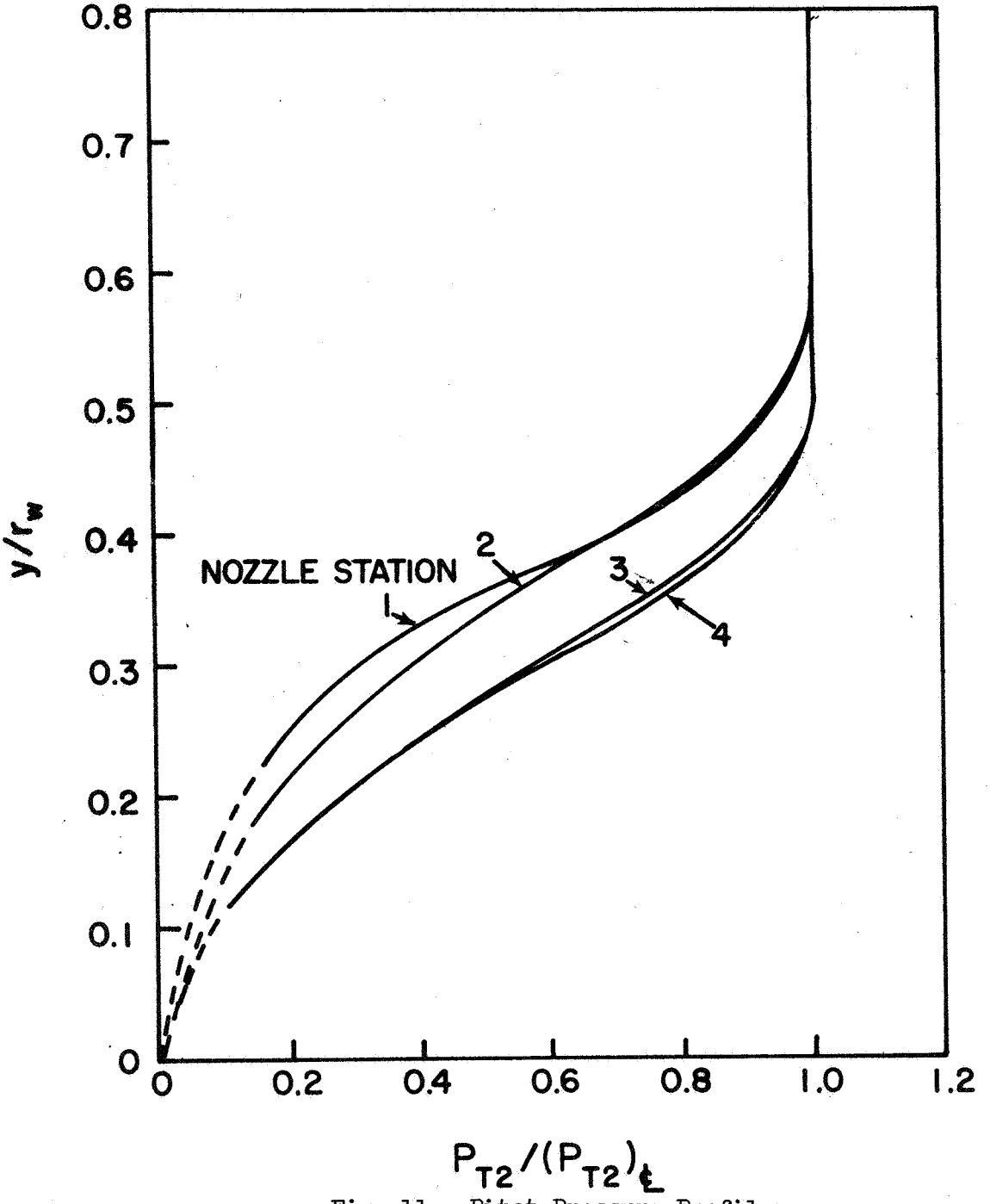

Fig. 11 - Pitot Pressure Profiles

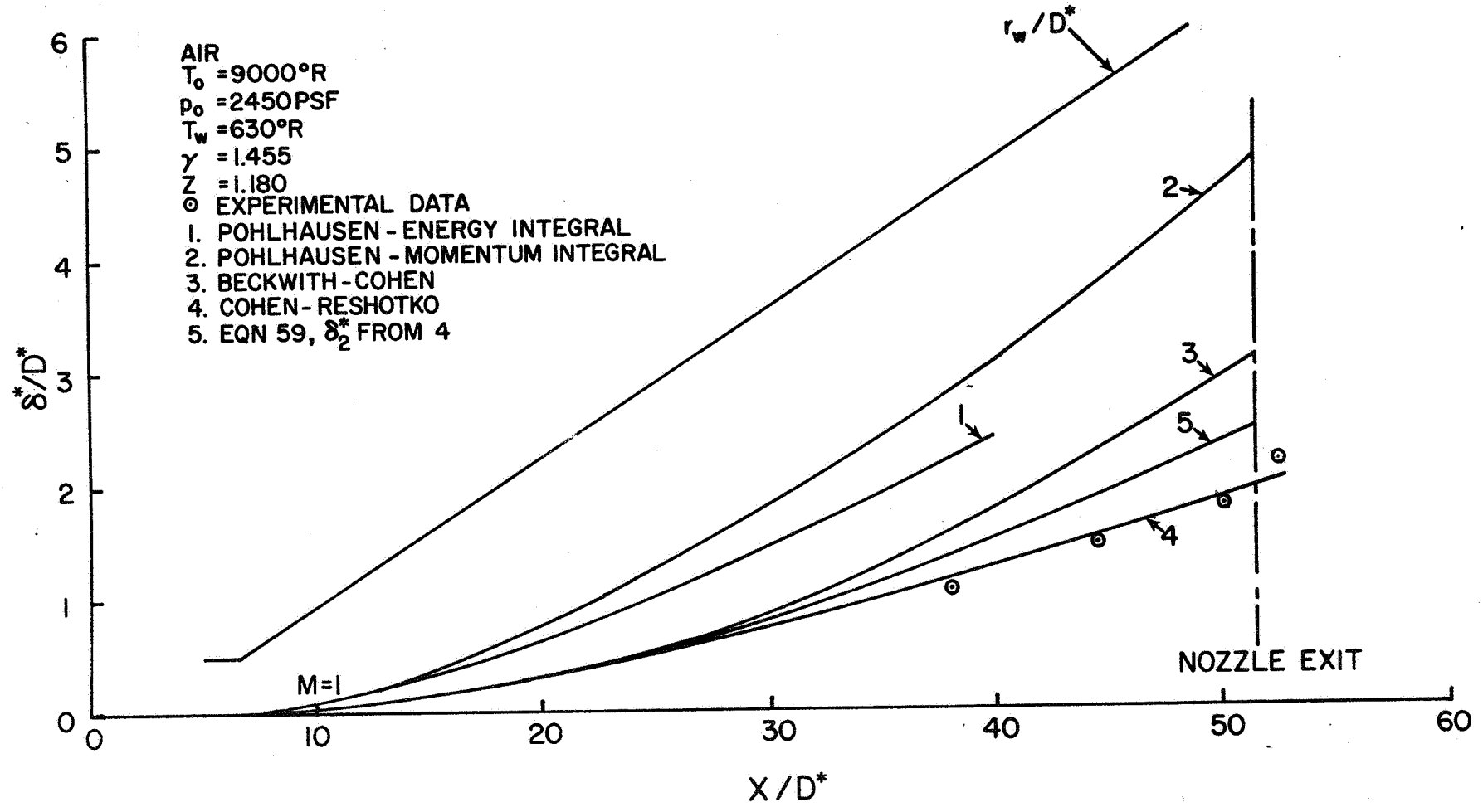

Fig. 12 - Boundary Layer Displacement Thicknesses

equation is employed; the momentum integral equation is used when skin friction results are required. Hence, the failure of the Beckwith-Cohen energy integral method to give accurate displacement thicknesses is not surprising.

The pressure gradient parameters resulting from the various techniques of analysis are compared in Fig. 12 for a typical set of wind-tunnel stagnation conditions. It is to be noted that the Beckwith-Cohen parameters are less than those of the other techniques. The smaller values for β influence the solution in the same manner as does a less favorable pressure gradient, leading to larger boundary layer thicknesses.

In Fig. 13 the β's obtained from the Cohen-Reshotko method are compared with those obtained by requiring strict mathematical similarity (Eq. 37.) The differences between these values of β are most significant in the region of the throat. In the supersonic flow, the β's from Eq. (37) would yield displacement thicknesses less than those obtained from the correlation of N versus n.

The agreement between the Cohen-Reshotko and the experimental thicknesses is shown in Fig. 12. In the Cohen-Reshotko calculations, six iterations of the solution were employed to account for the displacement interaction. It is to be noted that in the high Mach number regions of the expansion, the boundary layer comprised more than one-half of the nozzle flow field so that the interaction effects were extreme.

The displacement thicknesses calculated with Eq. (59), neglecting the effects of curvature on δ_2^*, are seen (Fig. 12) to over-estimate the actual thicknesses by nearly 20%. This demonstrates that the influence of curvature on δ_2^* can be significant. To examine this influence, δ_2^* was determined from the profile solution, including the curvature terms, with $P_R = 1$ and $c(x)$ scaled to yield the proper velocity thickness. With this revised value of δ_2^*, the displacement thickness was computed with Eq. (59). The various thicknesses are compared in Table II.

Table II - Boundary Layer Thicknesses at $x/D^* = 44.5$
$T_o = 4600°K$, $P_o = 1.2$ atm, $P_R = 1.0$

Case	δ^*/D^*	Remarks
1	1.450	Experimental
2	1.510	Cohen-Reshotko (δ_2^*/D^*)
3	2.26	Eq. (59) with δ_2^* of Case 2
4	1.288	Eq. (59) with δ_2^* from profile solutions

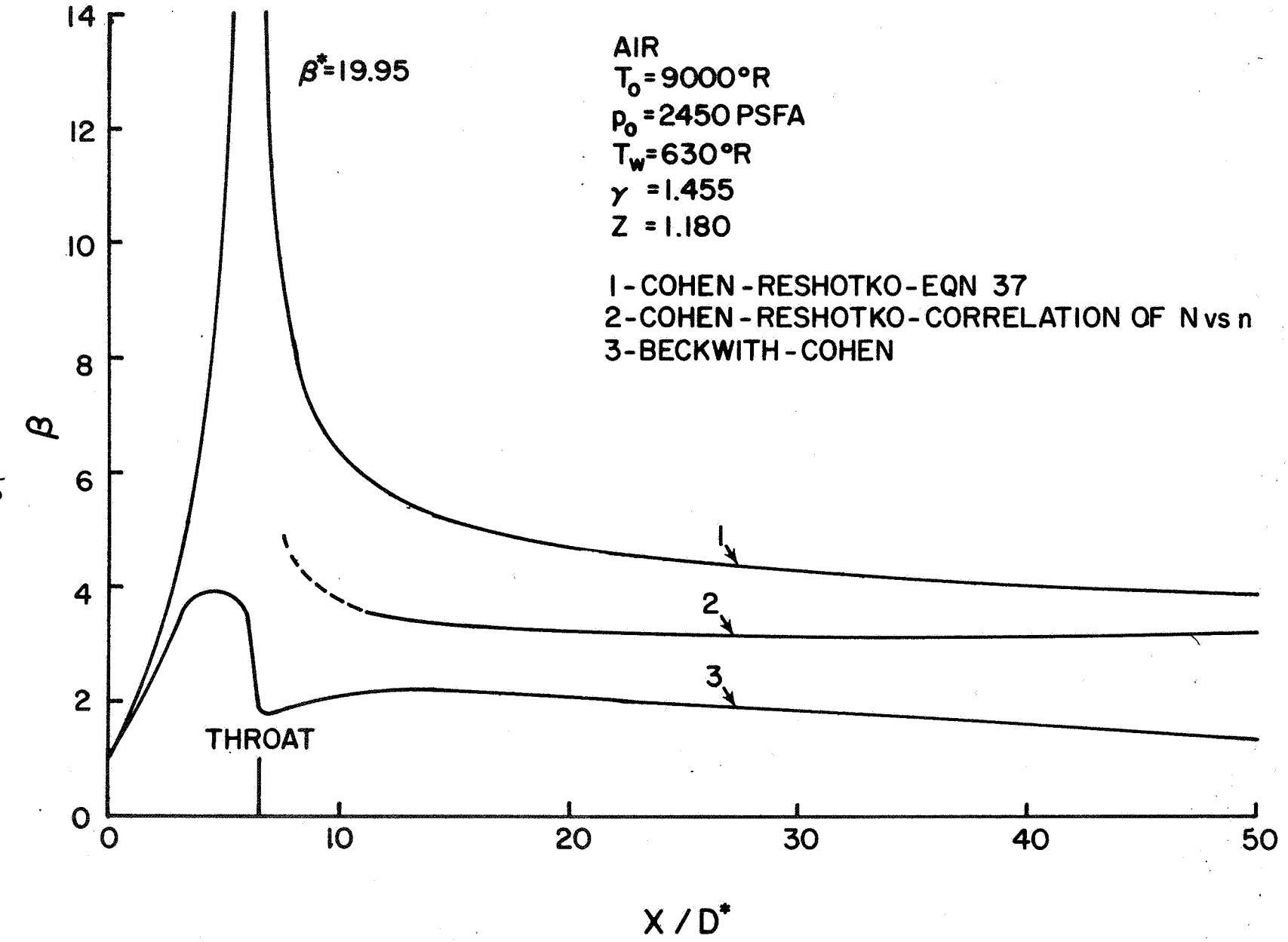

Fig. 13 - Pressure Gradient Parameters

The results summarized in Fig. 12 and Table II indicate that better agreement between the theoretical and experimental displacement thicknesses is obtained with a consistent treatment of the curvature effects. That is, the displacement thickness is set equal to δ_2^* when curvature is not included rather than using this δ_2^* in Eq. (59). Since universal profile solutions do not exist when the curvature terms are retained in the boundary layer equations, a consistent solution with curvature necessitates solving for the profiles. In this case, detailed numerical integration of the boundary layer equations would be required.

The method of Cohen and Reshotko over-estimates the boundary layer displacement thickness by approximately 4%. Hence, it is entirely satisfactory for predicting the thickness distributions in high-enthalpy nozzle flows. The technique yields data of sufficient accuracy to warrant using it for developing contours for parallel-flow nozzles or for determining the extent of displacement interaction in external flows. The improvements which might be offered by numerical integration of the boundary layer equations to account for transverse curvature, prior history, or the lack of similarity do not appear to justify the labor involved if only thickness information is desired. This may not be the case, however, for the determination of wall shear and heat transfer rates.

B. BOUNDARY LAYER PROFILES

The distributions of the rotational temperature of molecular nitrogen through the boundary layer obtained with the electron beam are shown in Fig. 14 and 15. The temperature surveys obtained over a range of stagnation enthalpies from 2000 to 6000 Btu/lb at a fixed axial location (Fig. 14) and those obtained at various axial stations (Fig. 15) show that the temperature profile is determined mainly by the wall temperature ratio. Profiles with nearly equal ratios of wall temperature and free-stream static temperature have the same shape when displayed in a nondimensional fashion. Since only minor variations in the boundary layer pressure gradient parameter is to be expected in the region of the flow field examined, the congruence of the temperature profiles with equal wall temperature ratios suggests that similarity in the boundary layer applies in the flow region.

The profiles in the free jet exhibit a shape difference from that obtained within the nozzle. As shown in Fig. 15, the temperature peak in the free-jet viscous layer is shifted toward the flow centerline. In addition, even though the free-jet data were obtained at a distance downstream of the nozzle exit equal to only 1/5 of a boundary layer thickness, the character of the profile near the outer edge of the jet (in the region near the nozzle wall) was significantly altered.

Some error in the nondimensional location of the free-jet temperature data is to be expected since it was impossible to define the exact location of the outer edge of the jet. For this reason, the radius of

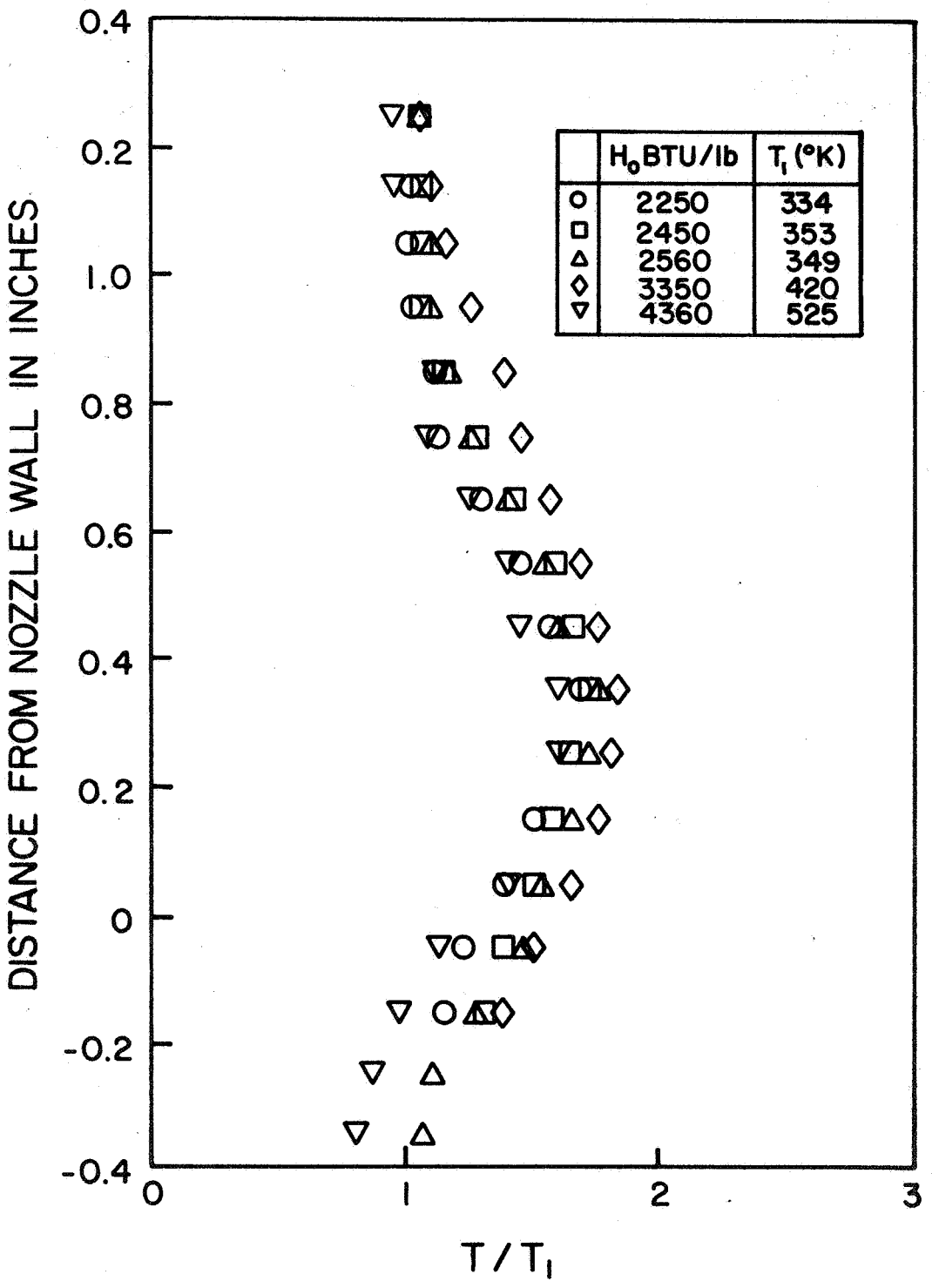

Fig. 14 - Static Temperature Profiles at Nozzle Station No. 1

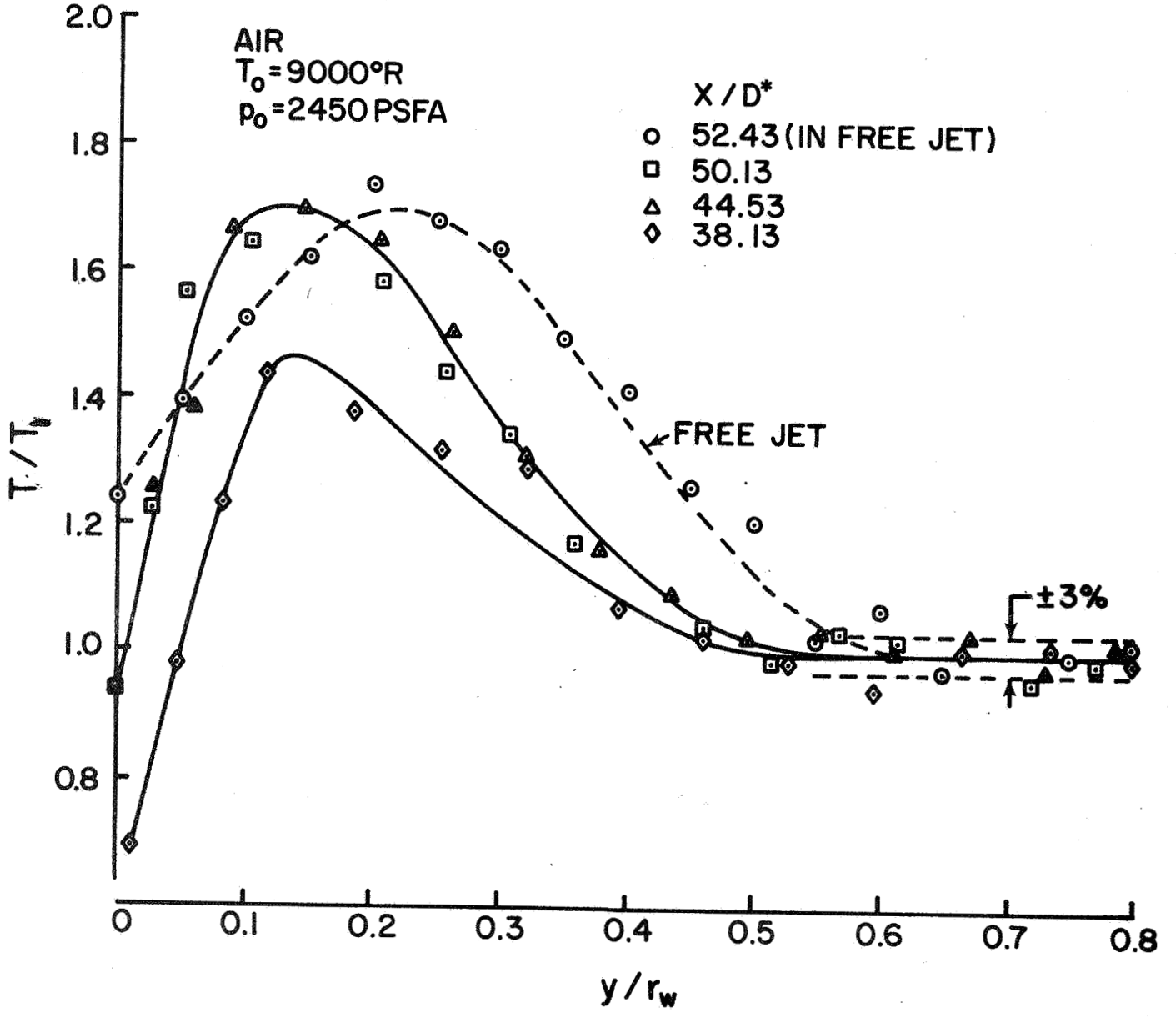

Fig. 15 - Static Temperature Surveys

the free jet was arbitrarily chosen equal to the nozzle-exit radius. A shift of the outer edge toward the nozzle centerline of approximately 0.10 inch would be required to bring the temperature peak to a nondimensional location equal to those of the other profiles. This shift would result in a flow turning angle at the wall of nearly 35° and would be accompanied by a strong exit shock wave system. None of the pitot pressure profiles indicate any measureable exit wave system (Fig. 11).

The change in the shape of the profile in the free jet is most probably related to the removal of the wall boundary conditions. The viscous layer examined actually was supported by a constant pressure boundary rather than by a solid wall so that the no-slip and wall-temperature conditions did not apply. Hence, this flow should be analyzed with techniques employed to study the nonsimilar regions of free shear layers.[21,22,23] There is no real reason to expect that the free-jet and boundary layer profiles will be identical.

The measured vibrational temperature profiles are shown in Fig. 16. It is to be noted that only a minor amount of vibrational relaxation occurs in the boundary layer, even in the region adjacent to the nozzle wall. Since vibrational relaxation is a two-body process, while chemical recombination generally requires three-body collisions, the lack of significant vibrational relaxation indicates that chemical recombination within the body layer was extremely unlikely.

An anomolous effect in the degree of vibrational relaxation is evident in Fig. 16. It is to be noted that in the region near the wall, the vibrational temperature of molecular nitrogen increases as the nozzle exit is approached. However, if the vibrational relaxation were a simple function of gas residence time, the trend of vibrational temperature near the wall shown in Fig. 16 would be reversed. That is, as the gas particles proceed through the flow field, the trend of vibrational relaxation should be toward equilibration of the translational and vibrational degrees of freedom. That is not the case, however, and there is an indication of a possible influence of the wall on the degree of vibrational relaxation which requires further study.

Detailed examination of the density profile was conducted at one axial station. The gas density ratio was determined with the mass flow probe. In addition, the local density ratio was determined by measuring the relative concentrations of molecular nitrogen with the electron beam. These profiles are compared with the reciprocal of the temperature profile in Fig. 17.

The density obtained with the electron beam is that of molecular nitrogen while the mass-flow probe yields total gas density. Although for the range of stagnation conditions examined molecular nitrogen acts as an inert dilutent, the agreement between the density profiles of Fig. 17 indicates that little chemical activity existed in the

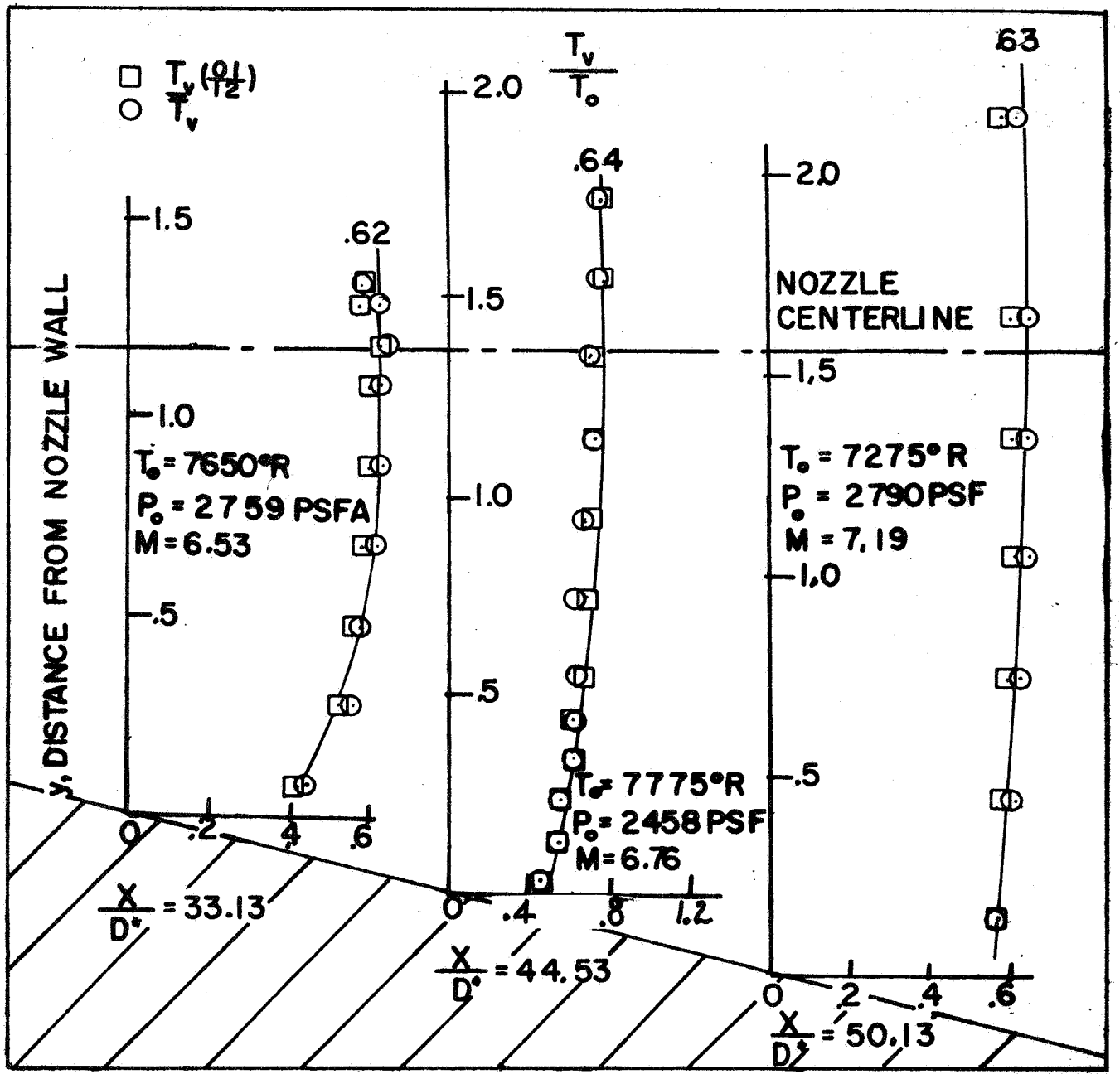

Fig. 16 - N_2 Vibrational Temperature Surveys

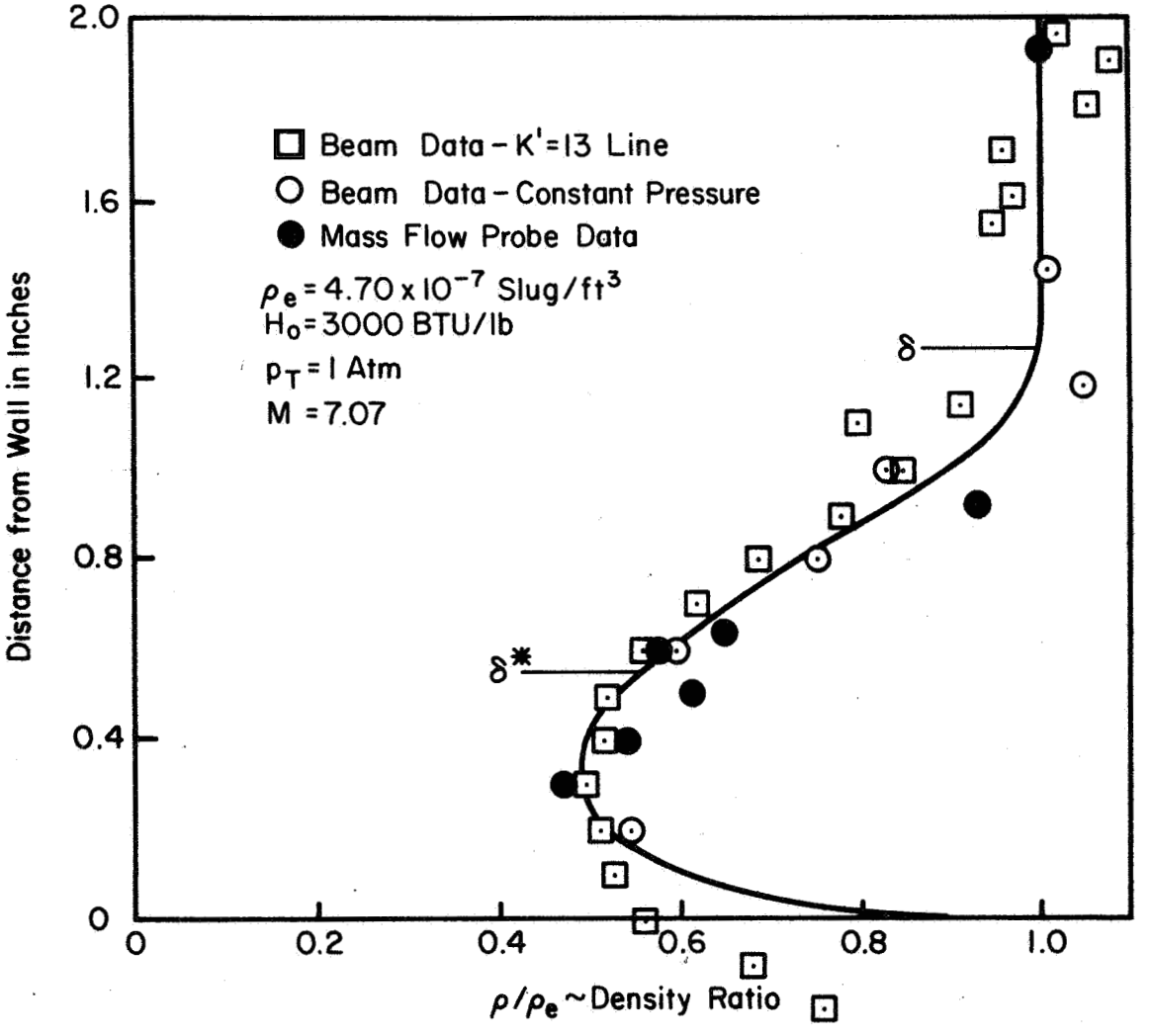

Fig. 17 - Density Profiles at Nozzle Station No. 1

boundary layer. In addition, the comparisons of the theoretical and experimental temperature profiles discussed in the following section show that the local static temperatures in the boundary layer were lower than those predicted by a perfect gas theory. If significant chemical recombination occurred in the boundary layer, it is likely that the measured temperature would be higher than the predicted values. The agreement of the density profiles evident in Fig. 17 and the small amount of vibrational relaxation indicated by the vibrational temperature data lead to the conclusion that there was no measureable chemical recombination within the boundary layer.

Typical nondimensional ρu profiles obtained with the mass flow probe are compared with the profiles obtained by combining the pitot pressure and temperature data (Eq. 106) in Fig. 18. The good agreement between the data obtained with the two techniques is apparent. The profiles obtained at all nozzle stations are summarized in Fig. 19. The profiles in the free jet reflect the different character of the viscous layer on a constant pressure boundary in agreement with the temperature data. The nondimensional velocity profiles within the nozzle are compared in Fig. 20.

The profiles obtained by combining the probe data could not be extended completely through the boundary layer. As the probe was moved toward the wall, the local pitot pressure decreased, reducing the pressure drop across the probe inlet. At pitot pressures below 5 mm Hg, the inlet shock-wave system was no longer "swallowed" by the probe so that the probe operation became subcritical causing the capture and inlet areas to be unequal. The location in the boundary layer corresponding to the occurrence of subscritical operation is easily recognized in data reduction by a sharp increase in the indicated flow velocity.

The experimental velocity and temperature profiles are compared with the theoretical profiles in Fig. 21 and 22. Since the probe comparisons at all nozzle stations are essentially identical, theoretical profiles are presented only for station 3.

Velocity and temperature profiles were computed for various values of the pressure gradient parameter. Computations were performed with Prandtl numbers of 1.0 and 0.7. Little variation in the velocity profile was obtained for values of the pressure gradient parameter ranging from zero to those obtained from the correlations of Cohen and Reshotko and from integration of the external flow parameters to force local similarity (Eq. 37).

The comparisons of the theoretical and experimental temperature profiles shown in Fig. 22 demonstrate that the temperature distribution shows much sensitivity to the technique of computation. It is particularly notable that the flat-plate temperature profiles ($\beta=0$) greatly over-estimate the peak temperature in the boundary layer. Since the flow gradients in the high Mach number regions of the

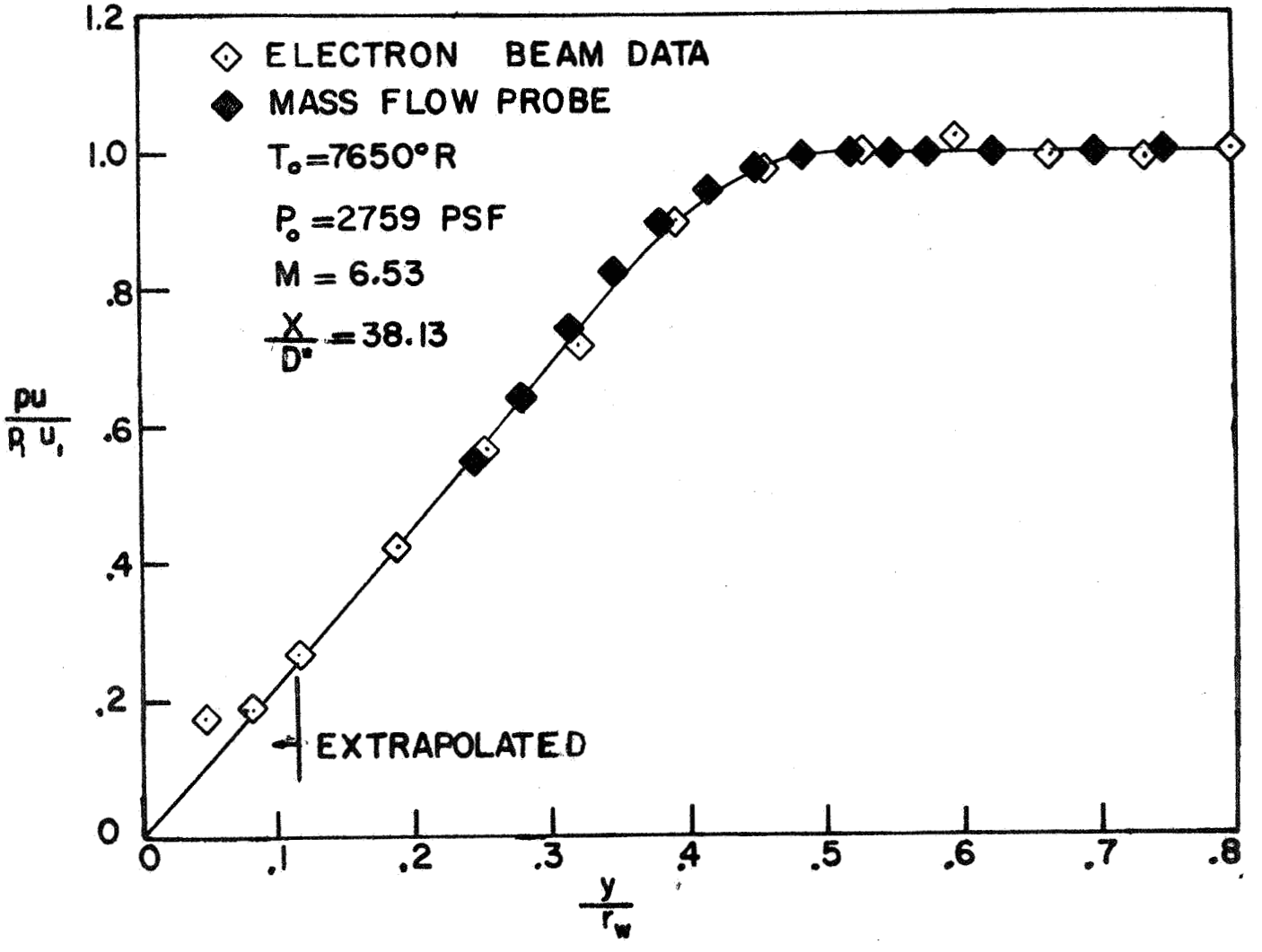

Fig. 18 - Mass Flow Profiles at Nozzle Station No. 4

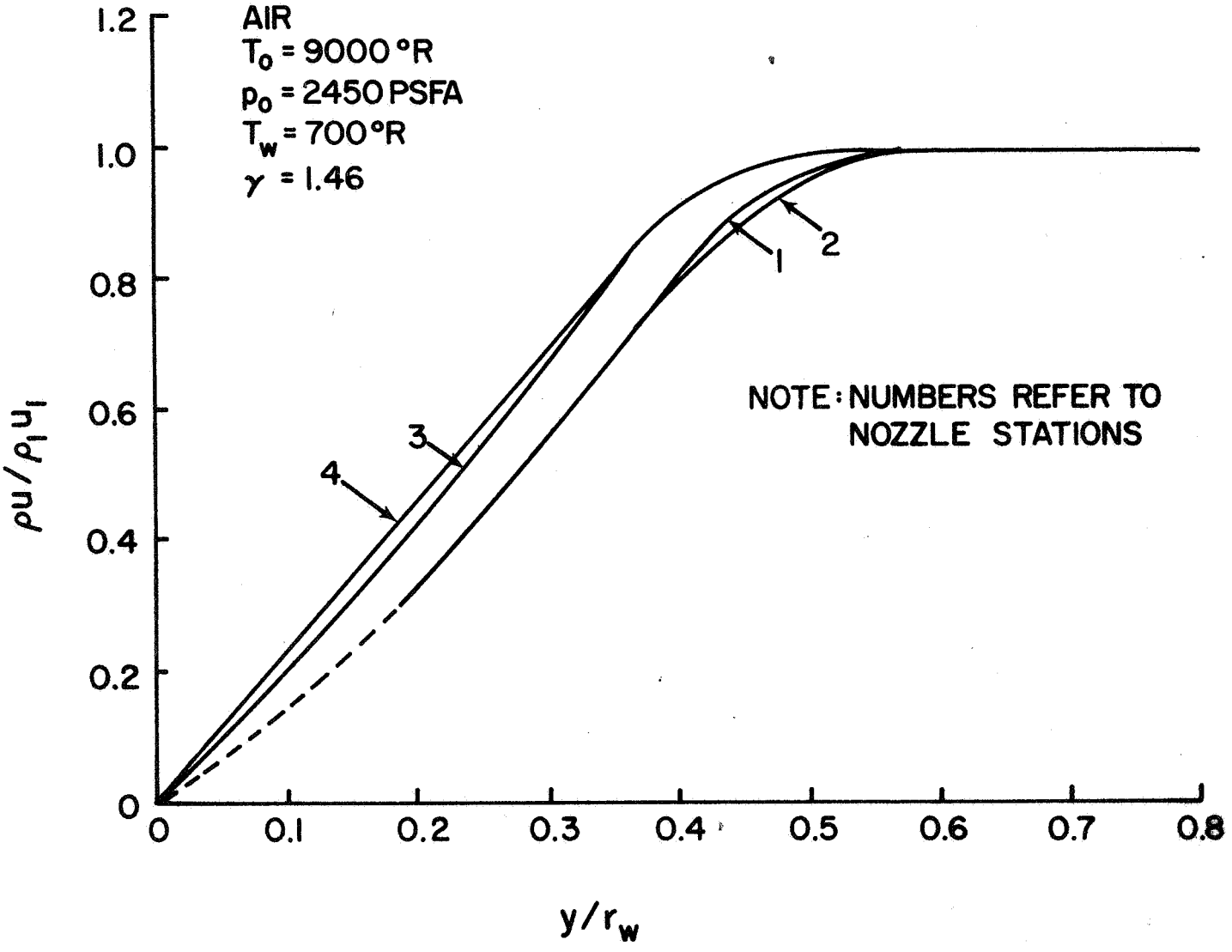

Fig. 19 - Mass Flow Profile Comparisons

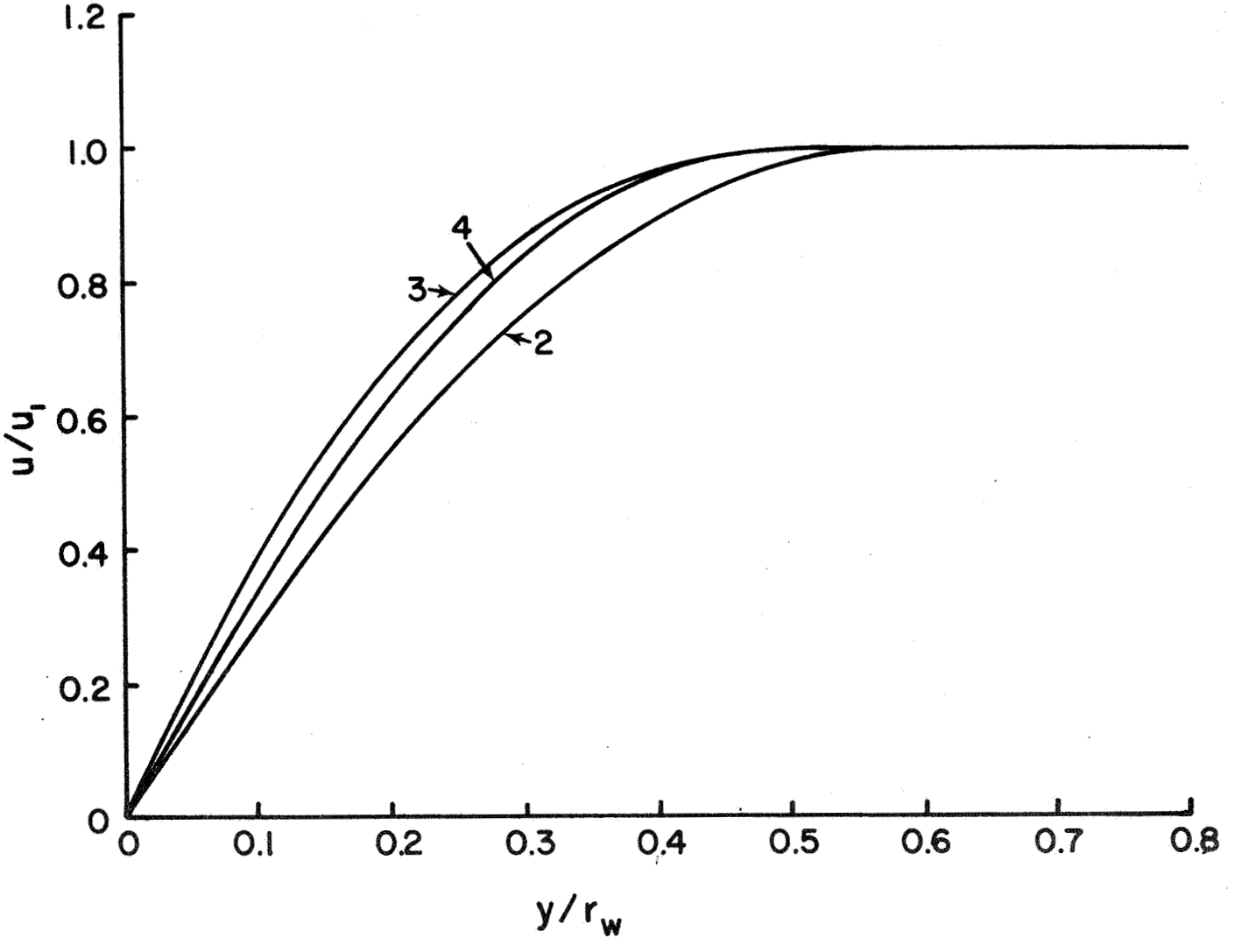

Fig. 20 - Velocity Profiles

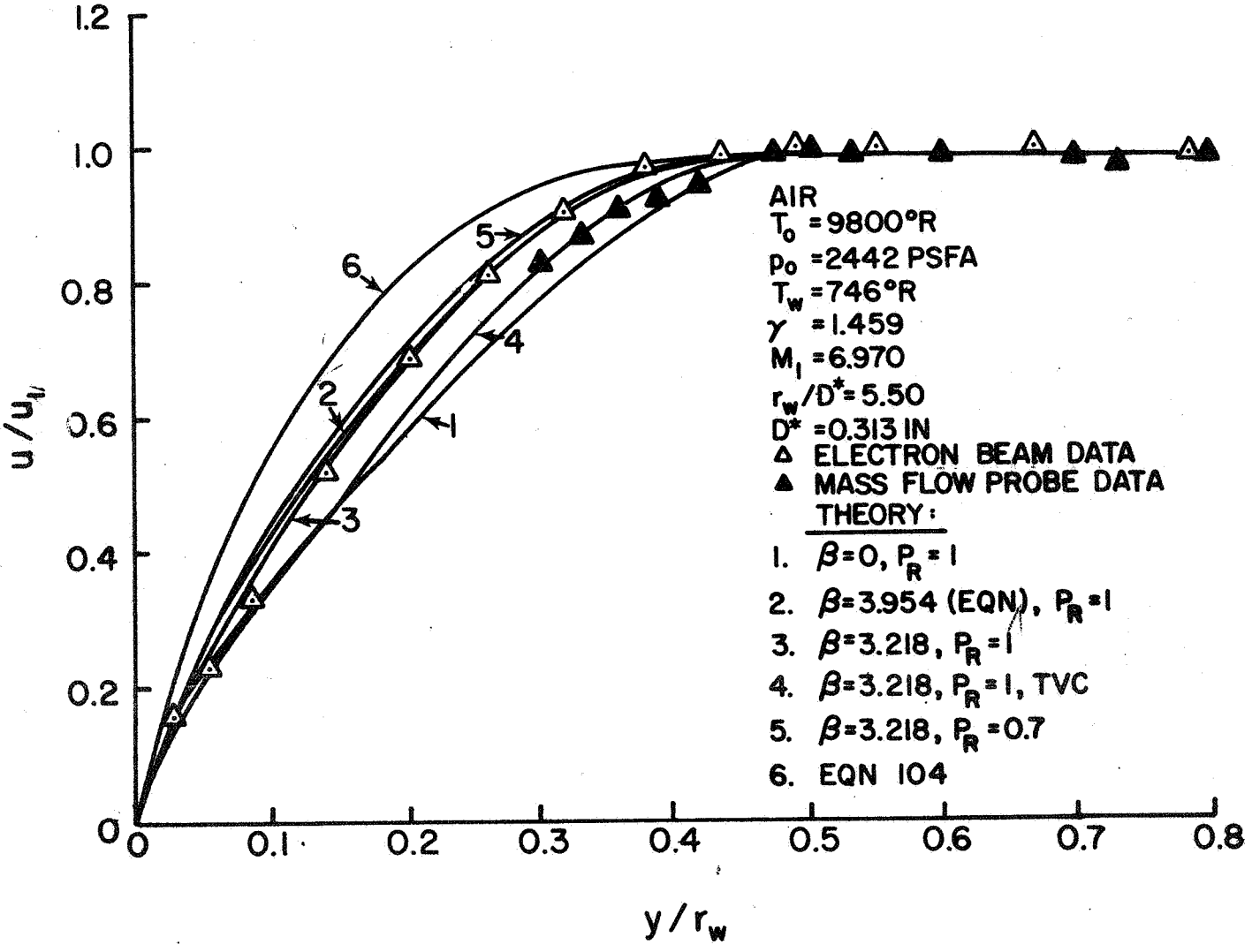

Fig. 21 - Velocity Profile Comparisons

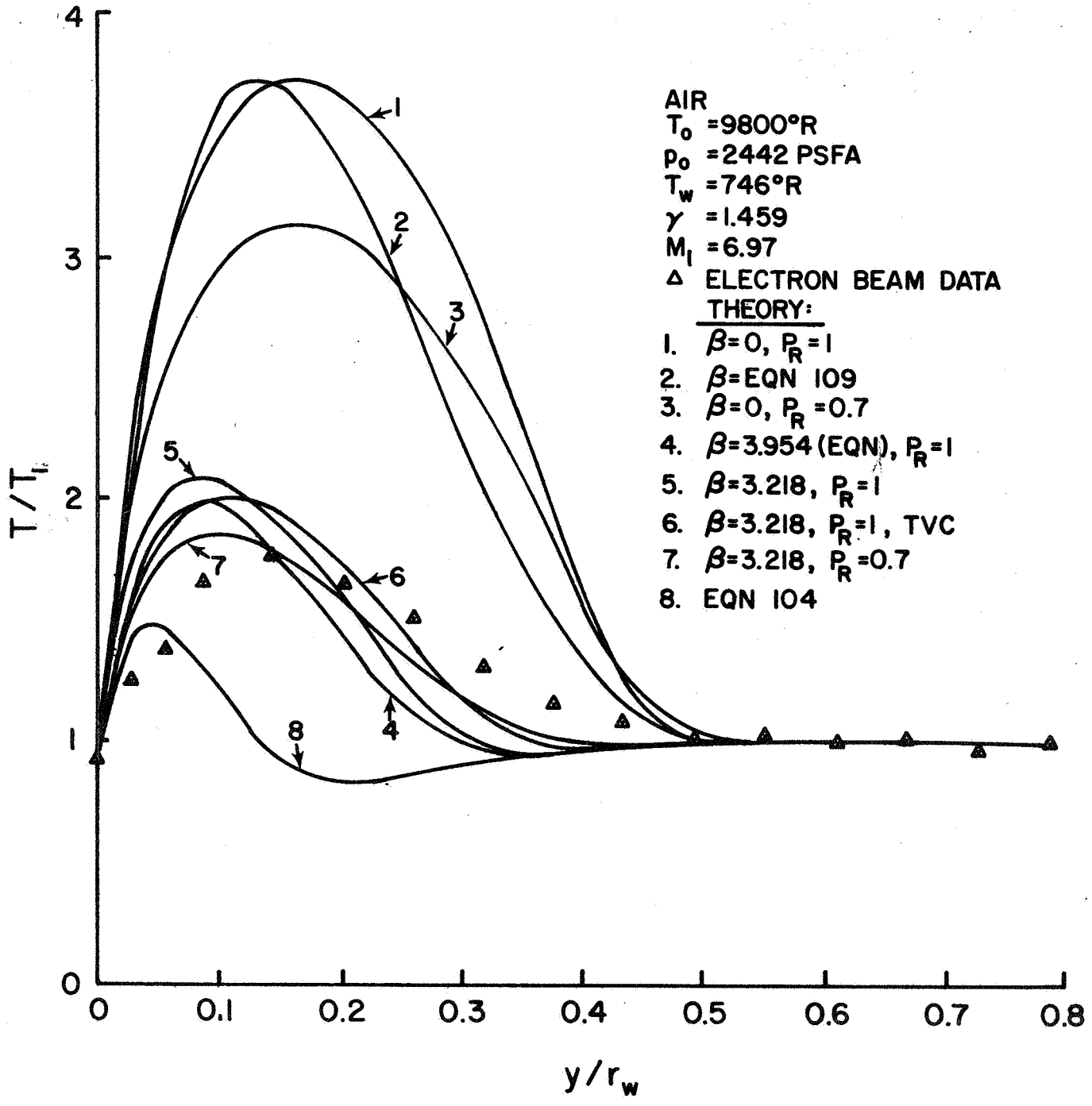

Fig. 22 - Temperature Profile Comparisons

expansion are small, it frequently is assumed that the temperature profile can be estimated with flat plate results. However, because of the large boundary layer thickness, the layer is characterized by a high pressure-gradient parameter and the flat plate theory clearly is not applicable.

Similar conclusions regarding the applicability of Crocco's equation can be reached from the temperature comparisons. When flat plate flow with $P_R = 1$ is assumed, the velocity and stagnation enthalpy profiles are related linearly in the form.

$$H = a + bu \quad , \tag{108}$$

from which is obtained

$$\frac{T}{T_1} = \frac{T_w}{T_1} + \left(1 - \frac{T_w}{T_1}\right)\frac{u}{u_1} + \frac{\gamma-1}{2} M_1^2 \left(1 - \frac{u}{u_1}\right)\frac{u}{u_1} \quad . \tag{109}$$

The experimental velocity ratios were used to evaluate T/T_1 from Eq. (109). It is readily observed in Fig. 22 that Crocco's equation gives a poor representation of the temperature profile.

The effect of transverse curvature is minor and is over-shadowed by the Prandtl number influences. The magnitude of the temperature peak is decreased by both curvature and decreasing Prandtl numbers. The temperature profile computed with a Prandtl number of 0.7 gives a better representation of the experimental temperature distribution, particularly in the regions near the outer edge of the layer.

The differences between the theoretical and experimental profiles shown in Fig. 21 suggest that the boundary layer is characterized by an extremely large pressure-gradient parameter. To examine the influence of large pressure-gradient paramenters, profiles were compared with the asymptotic solution of Coles[17] (Eq. 104 and 105). The asymptotic temperature profile is seen to give a poor representation of the overall temperature distribution. However, the asymptotic solution yields a temperature "undershoot" which appears to be characteristic of the similar solutions obtained with high pressure-gradient parameters. Examination of the profiles obtained from solution of Eq. (43-46) indicates a temperature undershoot which increases in magnitude as the value of the pressure-gradient parameter is increased. Inclusion of the transverse terms and nonunity Prandtl numbers reduce the undershoot.

The comparison between the profile computed with a Prandtl number of 0.7 and the experimental data is repeated in Fig. 23. In addition, the error band associated with the data is indicated. The error is based on a maximum uncertainity of ± 3% in the temperatures; the error limits shown in Fig. 23 correspond to the maximum deviation which could result from the temperature uncertainty.

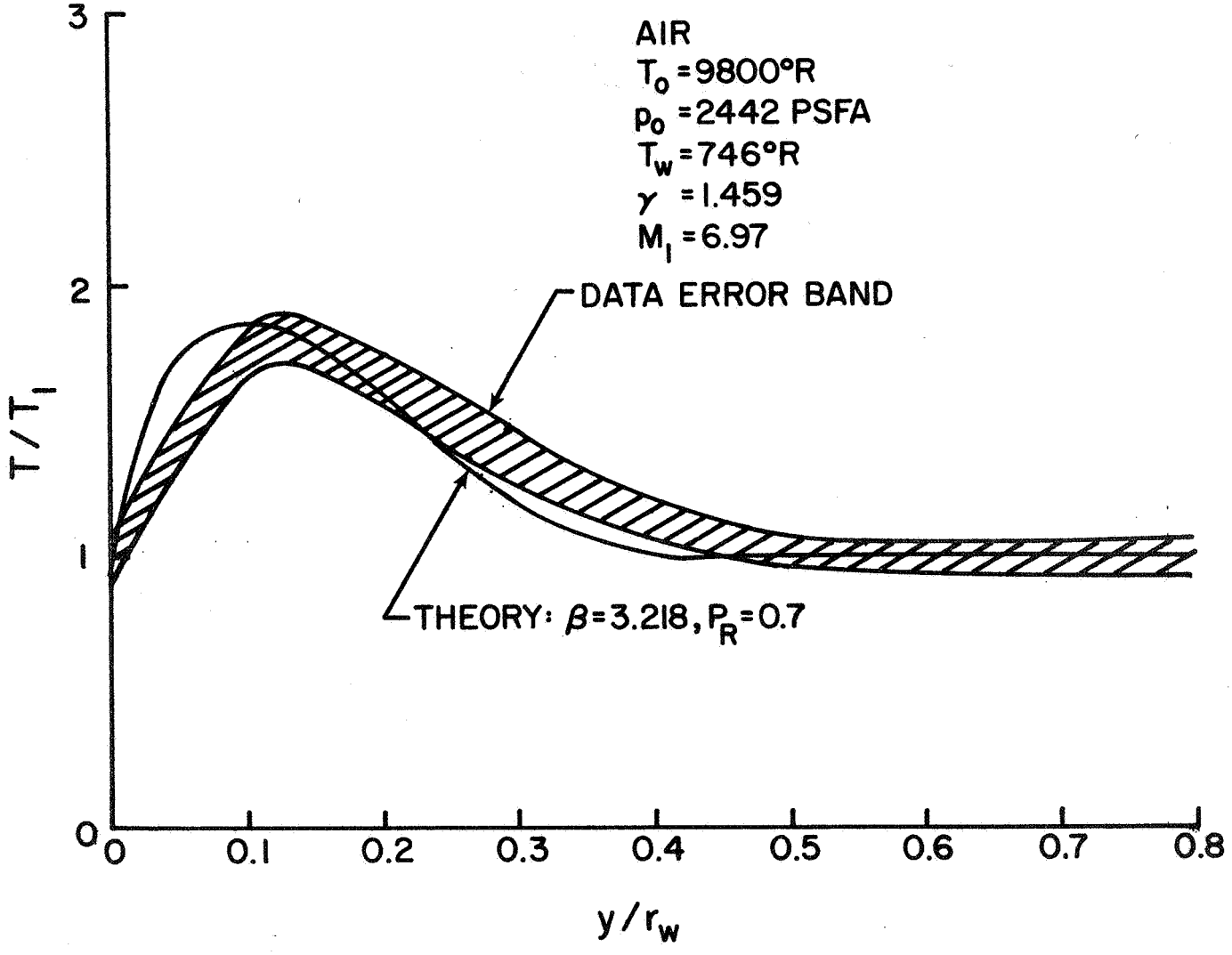

Fig. 23 - Theoretical and Experimental Temperature Profiles

The small difference between the experimental and theoretical profiles which remains after error analysis illustrates that in the high Mach number regions of the flow, a boundary layer theory employing the assumption of local similarity gives an accurate representation of the boundary layer profiles.

V. CONCLUSIONS

The method developed for predicting boundary layer thicknesses in high-enthalpy nozzle flows has proved completely adequate, even when the boundary layer comprises a major portion of the flow field. The influences of transverse curvature on the thickness distribution are minor. Pohlhausen methods and the energy integral technique of Beckwith and Cohen were found to over-estimate the thicknesses by large amounts.

For stagnation enthalpies from 2000 to 6000 Btu/lb at stagnation pressures near one atmosphere, no chemical recombination and little vibrational relaxation were found to occur within the boundary layer. However, an anomolous effect on the rate of equilibration of the vibrational and translational degrees of freedom for molecular nitrogen was obtained. More experimentation on the rate of vibrational relaxation near surfaces in high-enthalpy flows should be conducted to investigate the surface effects in more detail.

Comparisons of the theoretical and experimental boundary layer profiles demonstrate that a theory employing local similarity is adequate in the high Mach number regions of the expansion. Although in these regions the stream-wise gradients in flow properties are small, the large thickness causes the boundary layer to be characterized by a high value of the pressure-gradient parameter. Hence, flat plate theories were found to greatly over-estimate the peak temperature in the boundary layer.

The influence of transverse curvature in the boundary layer profiles was investigated. It was found that curvature must be included only to explain the finer features of the flow.

The similarity methods were found to be unsatisfactory in describing the structure of the viscous layer in the free jet. The removal of the wall temperature and no-slip conditions was found to be effective in altering the profiles, even at very small distances downstream of the nozzle exit. The results suggest that the viscous layer supported by a constant pressure boundary should not be examined with usual boundary layer theory.

The results reported here for high-enthalpy nozzle flows should be equally applicable in external flows. When the assumption of frozen chemistry can be applied, adequate boundary layer thicknesses can be obtained with the method of Cohen and Reshotko. In addition, boundary layer profiles can be predicted accurately when the proper values for the pressure-gradient parameter are used with the locally similar form of the boundary layer equations.

REFERENCES

1. Burke, A. F., and Bird, K. D., "The Use of Conical and Contoured Expansion Nozzles in Hypervelocity Facilities," paper presented at the Second Intern. Symposium on Hypervelocity Techniques, Denver, Colorado, March 10-20, (1962).

2. Edenfield, E. E., and Boudreau, A. H., "A Correlation of Boundary Layer Thickness and Displacement Thickness at Hypersonic Mach Numbers," paper presented to the Twenty-Sixth Supersonic Tunnel Association Meeting, NASA Ames Research Center, Moffett Field, Calif., September 26-27, (1966).

3. Luce, R., Gregorek, G. M.; and Lee, J. D., "The Laminar Boundary Layer in Axisymmetric Hypersonic Nozzle with Wall Cooling," The Ohio State University Aeronautical and Astronautical Research Laboratory, USAF ARL Report 65-112, (1965).

4. Cohen, C. B., and Reshotko, E., "The Compressible Laminar Boundary Layer with Heat Transfer and Arbitrary Pressure Gradient," NACA Report 1294, (1956).

5. Beckwith, I. E., and Cohen, N. B., "Application of Similar Solutions to Calculation of Laminar Heat Transfer on Bodies with Yaw and Large Pressure Gradient in High-Speed Flow," NASA TN D-625, (1961).

6. Clutter, D. W., and Smith, A. M. O., "Solution of the General Boundary Layer Equations for Compressible Laminar Flow, Including Transverse Curvature," Douglas Rept. LB 31088, (1964).

7. Smith, A. M. O., and Clutter, D. W., AIAA 4, 639, (1965).

8. Jaffe, N. A.; Lind, R. C.; and Smith, A. M. O., AIAA 9, 1563, (1967).

9. Petrie, S. L.; Pierce, G. A.; and Fishburne, E. S., "Thermochemical Analysis of an Expanded Air Plasma," The Ohio State University Aeronautical and Astronautical Research Laboratory, USAF AFFDL-TR-64-191, (1964).

10. Petrie, S. L., "Flow Field Analysis in a Low Density Arc-Heated Wind Tunnel," Proc. of 1965 Heat Transfer and Fluid Mechanics Institute, Stanford Univ. Press, (1965).

11. Petrie, S. L., and Pierce, G. A., "Boundary Layer Studies in Rarefied Plasma Flow," Rarefied Gas Dynamics, II, Academic Press, (1967).

12. Stewartson, K., Proc. Roy, Soc. of London, ser. A, 200, 84, (1949).

13. Yasuhara, M., J. Aerospace Sci. 29, 667, (1962).

14. Probstein, R. F., and Elliot, D., J. Aeronaut. Sci. 23, 208, (1956).

15. Hayes, W. D., and Probstein, R. F., Hypersonic Flow Theory, Academic Press, (1959).

16. Cohen, N. B., "Correlation Formulas and Tables of Density and Some Transport Properties of Equilibrium Dissociating Air for Use in Solutions of the Boundary Layer Equations," NASA TN D-194, (1960).

17. Coles, D., "The Laminar Boundary Layer Near a Sonic Throat," Proc. of 1957 Heat Transfer and Fluid Mechanics Institute, Stanford Univ. Press, (1957).

18. Petrie, S. L., AIAA 4, 1679, (1966).

19. Petrie, S. L., "Electron Beam Diagnostics," paper presented at AIAA Aerodynamic Testing Conference, Los Angeles, Calif., September 21-23, (1966).

20. Schlichting, H., Boundary Layer Theory, Fourth Edition, McGraw-Hill, (1961).

21. Lykoudis, P. S., AIAA 4, 577, (1966).

22. Chapman, D. R., "Laminar Mixing of a Compressible Fluid," NACA R-958, (1950).

23. Denison, M. R. and Baum, E., AIAA 1, 342, (1963).